OC-SMART: A machine learning based data analysis platform for satellite ocean color sensors

Yongzhen Fan [a,*], Wei Li [a], Nan Chen [a], Jae-Hyun Ahn [b], Young-Je Park [b], Susanne Kratzer [c], Thomas Schroeder [d], Joji Ishizaka [e], Ryan Chang [f], Knut Stamnes [a]

[a] Light & Life Laboratory, Department of Physics, Stevens Institute of Technology, Hoboken, NJ 07307, USA
[b] Korea Institute of Ocean Science and Technology, Korea Ocean Satellite Center, Busan 49111, Republic of Korea
[c] Department of Ecology, Environment and Plant Sciences (DEEP), Stockholm University, 106 91 Stockholm, Sweden
[d] CSIRO Ocean & Atmosphere, Brisbane, QLD 4001, Australia
[e] Institute for Space-Earth Environmental Research, Nagoya University, Nagoya, Japan
[f] Union County Magnet High School, Scotch Plains, NJ 07076, USA

ARTICLE INFO

ABSTRACT

We introduce a new platform, Ocean Color - Simultaneous Marine and Aerosol Retrieval Tool (OC-SMART), for analysis of data obtained by satellite ocean color sensors. OC-SMART is a multi-sensor data analysis platform which supports heritage, current, and possible future multi-spectral and hyper-spectral sensors from US, EU, Korea, Japan, and China, including SeaWiFS, Aqua/MODIS, SNPP/VIIRS, ISS/HICO, Landsat8/OLI, DSCOVR/EPIC, Sentinel-2/MSI, Sentinel-3/OLCI, COMS/GOCI, GCOM-C/SGLI, and FengYun-3D/MERSI2. The products provided by OC-SMART include spectral normalized remote sensing reflectances (R_{rs} values), chlorophyll_a (CHL) concentrations, and spectral in-water inherent optical properties (IOPs) including absorption coefficients due to phytoplankton (a_{ph}), absorption coefficients due to detritus and Gelbstoff (a_{dg}) and backscattering coefficients due to particulates (b_{bp}). Spectral aerosol optical depths (AODs) and cloud mask results are also provided by OC-SMART.

The goal of OC-SMART is to improve the quality of global ocean color products retrieved from satellite sensors, especially under complex environmental conditions, such as coastal/inland turbid water areas and heavy aerosol loadings. Therefore, the atmospheric correction (AC) and ocean IOP algorithms in OC-SMART are driven by extensive radiative transfer (RT) simulations in conjunction with powerful machine learning techniques.To simulate top of the atmosphere (TOA) radiances, we solve the radiative transfer equation pertinent for the coupled atmosphere-ocean system. For each sensor, we have created about 13 million RT simulations and comprehensive training datasets to support the development of the machine learning AC and in-water IOP algorithms. The results, as demonstrated in this paper, are very promising. Not only does OC-SMART improve the quality of the retrieved water products, it also resolves the negative water-leaving radiance problem that has plagued heritage AC algorithms. The comprehensive training datasets created using multiple atmosphere, aerosol, and ocean IOP models ensure global and generic applicability of OC-SMART.

The use of machine learning algorithms makes OC-SMART roughly 10 times faster than NASA's SeaDAS platform. OC-SMART also includes an advanced cloud screening algorithm and is resilient to the contamination by weak to moderate sunglint and cloud edges. It is therefore capable of recovering large amounts of data that are discarded by other algorithms (such as those implemented in NASA's SeaDAS package), especially in coastal areas. OC-SMART is currently available as a standalone Python package or as a plugin that can be installed in ESA's Sentinel Application Platform (SNAP).

* Corresponding author.
E-mail address: yfan@stevens.edu (Y. Fan).

1. Introduction

After a successful proof-of-concept mission using CZCS (1978–1986), SeaWiFS (1997–2010), MODIS (1999-present), MERIS (2002−2012), and VIIRS (2012-present) for over 20 years, have provided a global view of many useful products representing optical in-water constituents of natural waters such as chlorophyll-a, especially in open ocean areas where the dominant absorbers and scatterers of light in surface waters are phytoplankton. It is still very challenging, however, to retrieve in-water products from optically-complex environments such as coastal areas, where approximately 50% of the world's human population live and generate about 46% of global economic activity. Coastal waters are characterized by a myriad of complex interactions among human activities, biogeochemical cycles, and physical dynamics. Highly absorbing dissolved organic matter and absorbing and scattering organic and inorganic particles dominate coastal waters and can be independent of the coastal phytoplankton community. In shallow coastal waters, re-suspended sediments and other particulates scatter light, contribute to the water-leaving radiance. Heavily polluted continental aerosols and sand storms also frequently impact coastal areas and make the retrieval of water constituents from satellite measurements difficult.

In order to retrieve information about water constituents from satellite ocean color measurements, the contribution from the Earth's atmosphere (i.e., molecules, aerosols etc.) must be taken into account. Heritage atmospheric correction (AC) algorithms (Gordon and Wang, 1994b; Gordon, 1997) used by the ocean color community, describe the radiance at wavelength λ measured by a satellite ocean color sensor at the top of the atmosphere (TOA) as:

$$L_t(\lambda) = L_r(\lambda) + L_a(\lambda) + T(\lambda)L_g(\lambda) + t(\lambda)L_{wc}(\lambda) + t(\lambda)L_w(\lambda) \tag{1}$$

where L_t is the total radiance, L_r is the radiance contributed by molecular (Rayleigh) scattering (Gordon and Wang, 1992; Wang, 2002, 2005), L_a is the radiance contributed by aerosol scattering/absorption including aerosol-Rayleigh interactions, L_g is the radiance contributed by sunglint (Wang and Bailey, 2001), L_{wc} is the radiance contributed by surface whitecaps (Gordon and Wang, 1994a; Frouin et al., 1996; Stramska and Petelski, 2003), and L_w is the upward radiance in the water transmitted through the water-atmosphere interface, commonly referred as the water-leaving radiance. T and t are atmospheric direct and diffuse transmittances. The heritage AC algorithms evaluate each of the terms (i.e. L_r, L_a, L_g, and L_{wc}) carefully and remove them from L_t to produce L_w.

A coupled atmosphere-ocean radiative transfer model (RTM) with full consideration of multiple scattering effects and the interaction between the atmosphere and ocean should be used for accurate simulations of satellite sensor measurements, and the inverse problem needs to be reformulated to be consistent with the forward modeling approach. Therefore, a new algorithmic approach is needed for optically-complex atmospheric and coastal conditions. Fan et al. (2017) developed a new AC algorithm for MODIS based on coupled atmosphere-ocean RT simulations (Stamnes et al., 2018a) combined with multilayer neural networks (MLNNs). This new AC algorithm completely resolved the negative water-leaving radiance issue and the validation of the algorithm showed significant improvement in blue and red bands when compared with the latest heritage algorithms, which included NIR water-leaving radiance corrections and use of SWIR bands to estimate the aerosol contribution to the signal.

Although the Fan et al. (2017) AC algorithm focused on coastal areas, the forward/inverse modeling framework created should be applicable globally. Therefore, in this paper, we present the methodology and validation of a new global approach to AC as well as aerosol and water IOP retrievals. We use a coupled atmosphere-ocean RTM (Stamnes et al., 2018a) to generate comprehensive global ocean color datasets. These simulated datasets are in turn used to train a machine learning based water IOP retrieval algorithm validated against in-situ measurements on a global scale. The new global AC and ocean IOP algorithms have been implemented in our multi-sensor data analysis platform, Ocean Color - Simultaneous Marine and Aerosol Retrieval Tool (OC-SMART), which currently supports ocean color data retrievals from 11 satellite sensors including: SeaWiFS, Aqua/MODIS, SNPP/VIIRS, ISS/HICO, Landsat8/OLI, DSCOVR/EPIC, Sentinel-2/MSI, Sentinel-3/OLCI, COMS/GOCI, GCOM-C/SGLI and FengYun-3D/MERSI. OC-SMART is available for download from the Light and Life Lab website (http://www.rtatmocn.com/oc-smart/) as a standalone Python package and also as a plugin that can be installed in ESA's SNAP platform.

2. Machine learning based AC and ocean IOP algorithms

2.1. Brief description of forward radiative transfer model

To simulate TOA radiances, we will not rely on Eq. (1), but instead solve the radiative transfer equation (RTE) for the diffuse radiance $L(\tau, u, \phi)$

$$u\frac{dL(\tau, u, \phi)}{d\tau} = L(\tau, u, \phi) - \overbrace{\frac{\varpi(\tau)}{4\pi}\int_0^{2\pi}d\phi'\int_{-1}^1 du' p(\tau, u', \phi'; u, \phi)L(\tau, u', \phi')}^{\text{multiple scattering}} - \overbrace{\frac{\varpi(\tau)}{4\pi}p(\tau, -\mu_0, \phi_0; u, \phi)F_0 e^{-\tau/\mu_0}}^{\text{single scattering}}. \tag{2}$$

Analyses based on Eq. (1) have been successfully applied to various ocean sensors to produce ocean color products with satisfactory results, especially in open ocean areas. However, due to the lack of accurate and efficient algorithms for radiative transfer simulations in a fully coupled atmosphere-ocean system, some underlying assumptions had to be made in Eq. (1). These assumptions work well for open ocean and weakly absorbing aerosol conditions, but become invalid in complex environmental conditions, such as coastal/inland water areas, polluted aerosols, etc. As a result, the quality of ocean color products derived from the heritage approach based on Eq. (1), is often less than satisfactory in coastal regions and sometimes yields unphysical negative water-leaving radiances. There are a number of reasons for this predicament including use of a pre-defined set of aerosol models, inadequate knowledge of bio-optical properties in the NIR, the assumed vertical structure, etc. (IOCCG, 2019).

pertinent for the coupled atmosphere-water system. Here u is the cosine of the polar angle θ, ϕ is the azimuth angle, μ_0 is the cosine of the solar zenith angle, $\varpi(\tau) = b(\tau)/[a(\tau) + b(\tau)]$ is the single-scattering albedo, $a(\tau)$ is the absorption coefficient, $b(\tau)$ is the scattering coefficient, $p(\tau, u', \phi'; u, \phi)$ is the scattering phase function, and F_0 is the extraterrestrial solar irradiance. The differential vertical optical depth is given by $d\tau(z) = -[a(\tau) + b(\tau)]dz$.

We assume that the stratified atmosphere-water system can be adequately represented by two adjacent horizontal slabs across which the refractive index changes from its value in air to that in water. The numerical code AccuRT (Stamnes et al., 2018a) computes radiances at any optical depth, polar, and azimuth angle by solving Eq. (2) for each layer of the two slabs using the discrete-ordinate method to convert the integro-differential RTE into a system of coupled ordinary differential equations. The AccuRT method can be summarized as follows:

1. Slab$_1$ (air) and slab$_2$ (water) are separated by a plane interface at which the refractive index changes from m_1 in slab$_1$ to m_2 in slab$_2$, where m_2 depends on the wavelength.
2. Each of the two slabs is divided into a sufficiently large number of homogeneous horizontal layers to adequately resolve the vertical variation in its IOPs.
3. Fresnel's equations for the reflectance and transmittance are applied at the air-water interface, in addition to the law of reflection and Snell's Law to determine the magnitude and directions of the reflected and refracted rays.
4. Discrete-ordinate solutions to the RTE are computed for each layer in the two slabs.
5. Finally, boundary conditions at the top of slab$_1$ (TOA) and the bottom of slab$_2$ (water column) are applied, in addition to radiance continuity conditions at layer interfaces within each of the two slabs.

The air-water interface is assumed to be smooth in the simulations used to create the training data for the current version of OC-SMART. Use of a smooth air-water interface in this paper implies that the glint reflection will be strictly in the specular direction, but we consider only the diffuse part of the reflected light that has been subject to multiple scattering on its path from the surface to the TOA. We will refer to this contribution as 'moderate' sunglint. In other words, the part of the sunglint that is directly transmitted to the TOA, referred to as 'strong' sunglint, is not included in this treatment, but all orders of 'skyglint' (i.e. downward diffuse light specularly reflected by the air-water interface) are fully accounted for (see Ottaviani et al. (2008) for details).

2.2. Overview of the machine learning methodology

The methodology of the machine learning based AC algorithm, developed for MODIS and described in detail by Fan et al. (2017), is summarized here. The algorithm exploits the spectral similarity between the Rayleigh-corrected TOA radiance ($L_{rc} = L_t - L_r$) and the water-leaving radiance (L_w). A well-trained multilayer neural network is used to derive L_w from L_{rc} directly. Therefore, in contrast to heritage algorithms which tend to rely on accurate evaluation of the aerosol contribution to the radiance (L_a), our machine learning based AC algorithm is a spectral matching algorithm which does not depend on explicit evaluation of aerosol information. A secondary MLNN was also trained to derive spectral aerosol optical depths (AODs) from L_{rc} directly. The framework adopted to generate the MLNNs is shown in Fig. 1. In general, this framework can be applied generically, i.e. to any sensor with a suitable combination of bands. In particular, it is applicable to sensors, such as DSCOVR/EPIC, that do not have NIR or SWIR bands which are often required by heritage algorithms to estimate the aerosol contribution to the TOA sensor signal. The keys to the success of the machine learning based AC algorithm implemented in OC-SMART

can be summarized as follows:

- Extensive RT simulations from a coupled atmosphere-ocean RTM (Stamnes et al., 2018a) accurately accounts for multiple scattering and BRDF effects between the atmosphere and the ocean.
- Flexible water IOP models and aerosol models are used in the RT simulations to create a comprehensive dataset of L_{rc} and L_w values that are representative of most water and aerosol conditions encountered globally.
- Realistic input parameter distributions for the aerosol and water IOP models are obtained by analyzing level-3 global ocean color products from current ocean color sensors.
- A one-step process is employed that uses spectral features from visible (VIS) and near infrared (NIR) wavelengths simultaneously.
- The OC-SMART approach is capable of handling noise in the satellite measurements and it includes full consideration of the signal-to-noise ratio (SNR) characteristics of the sensor.

This framework is used to develop a new AC algorithm that is applicable globally. However, a global application requires comprehensive RT simulation datasets that are representative of different types of atmospheric, aerosol, and marine conditions in both open ocean and coastal areas. Therefore, careful modifications to our RT model simulations, the training datasets, and the training method have been made, which will be discussed in the following sections in some detail.

2.3. Atmospheric profiles and aerosol models

Fan et al. (2017) used the U.S. standard atmospheric profile for the simulation of molecular (Rayleigh) scattering and absorption by atmospheric gases. For the global application, we use the six atmospheric profiles, implemented in AccuRT, our coupled atmosphere-ocean RTM (Stamnes et al., 2018a), including U.S. standard, Mid-latitude summer&winter, sub-arctic summer&winter and tropical models. These atmospheric profiles are randomly selected for each RT simulation. A spectral band model (Kneizys et al., 1996) is used to compute the IOPs of atmospheric gas absorption and the relative spectral response functions appropriate for each sensor are used to compute the band-averaged values of the IOPs. The Rayleigh scattering phase function is given by (Stamnes et al., 2018a)

$$p_{Ray}(cos\Theta) = \frac{3}{3+f}\left(1 + fcos^2\Theta\right) \tag{3}$$

where Θ is the scattering angle and $f = \frac{1-\rho}{1+\rho}$. For air molecules the depolarization factor (attributed to the anisotropy of the scatterer, see Eq. (63) in Stamnes and Stamnes (2016) for a definition) has the value $\rho = 0.0286$ at 500 nm (Bodhaine et al., 1999).

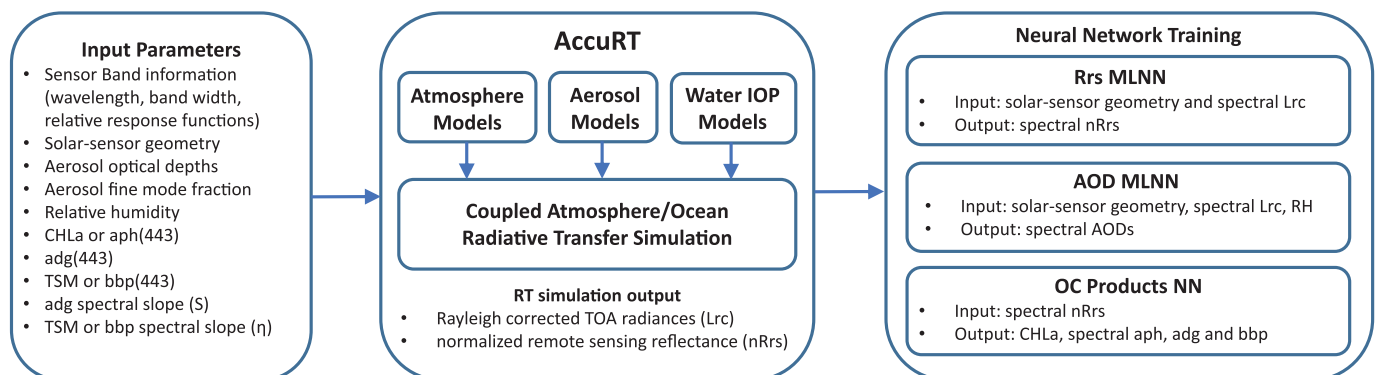| **Input Parameters**	**AccuRT**	**Neural Network Training**
• Sensor Band information (wavelength, band width, relative response functions) • Solar-sensor geometry • Aerosol optical depths • Aerosol fine mode fraction • Relative humidity • CHLa or aph(443) • adg(443) • TSM or bbp(443) • adg spectral slope (S) • TSM or bbp spectral slope (η)	**Atmosphere Models** **Aerosol Models** **Water IOP Models** **Coupled Atmosphere/Ocean Radiative Transfer Simulation** **RT simulation output** • Rayleigh corrected TOA radiances (Lrc) • normalized remote sensing reflectance (nRrs)	**Rrs MLNN** • Input: solar-sensor geometry and spectral Lrc • Output: spectral nRrs **AOD MLNN** • Input: solar-sensor geometry, spectral Lrc, RH • Output: spectral AODs **OC Products NN** • Input: spectral nRrs • Output: CHLa, spectral aph, adg and bbp

Fig. 1. Framework employed to develop the AC and ocean IOP inversion algorithms using accurate and comprehensive RT simulation datasets and multilayer neural networks.

The aerosol models used to develop the machine learning based global AC algorithms were proposed by Ahmad et al. (2010) based on Aerosol Robotic Network (AERONET) observations (Holben et al., 1998). The inherent optical properties (IOPs, i.e. absorption and scattering coefficients and the scattering phase functions) of the aerosol particles are computed from Mie scattering theory based on particle size distributions and refractive indices which vary with aerosol type and relative humidity (RH). These aerosol models are also used to generate aerosol radiance (L_a) look-up-tables (LUTs) for the heritage algorithm implemented in NASA's SeaDAS platform. However, the Ahmad models include only weakly absorbing aerosols with single-scattering albedo (ϖ) larger than 0.94. Comparing the Ahmad models with the aerosol models in the OPAC 4.0b package (Koepke et al., 2015), we found that only continental clean and maritime clean aerosol can be represented by the Ahmad models, as is expected, because they were derived mainly from data obtained at open ocean AERONET stations. Only three coastal AERONET stations in Chesapeake Bay were included, where the aerosols are not heavily polluted. Therefore, the Ahmad models lack representativeness in some coastal areas (Pahlevan et al., 2017a). In order to have a better representation of coastal areas that are often invaded by heavily polluted aerosols and sand storms, such as the East China Sea and the west coast of Africa, we have, in addition to the Ahmad aerosol models, incorporated the polluted Continental aerosol, the polluted Maritime aerosol, and the desert aerosol models, from the OPAC package (Koepke et al., 2015), into our RT simulations.

2.4. Flexible and comprehensive ocean IOP models

The inherent optical properties (IOPs) of the open ocean and various types of coastal/inland waters are all different. However, the IOPs of the water, i.e., the total absorption coefficient $a_t(\lambda)$ and the total scattering coefficient $b_t(\lambda)$, will generally have contributions from water itself and water constituents, including embedded particles (i.e. phytoplankton, detritus, minerals etc.), and colored dissolved organic matter (CDOM). For pure water, we use the absorption coefficient $a_w(\lambda)$ based on data published by Pope and Fry (1997) for wavelengths between 400 and 700 nm, and by Kou et al. (1993) for wavelengths between 700 and 900 nm. The scattering coefficient of water $b_w(\lambda)$ is based on data published by Smith and Baker (1981) and the Rayleigh scattering phase function (see Fig. 1 in supplementary material available online) is given by Eq. (3) with a depolarization factor of $\rho = 0.039$ for water. The sensor-specific relative spectral response functions were used to compute band-averaged absorption and scattering coefficients for pure water.

The IOPs of the water constituents are usually derived from bio-optical models (BOMs). However, there is no single BOM capable of simulating the IOPs for all possible marine conditions over the global ocean including coastal areas. Therefore, multiple BOMs are needed to create a comprehensive and representative global water IOP dataset. We implemented three BOMs for our RT simulations: the modified GSM model (Fan et al., 2017; Garver and Siegel, 1997; Maritorena et al., 2002), the modified CCRR model (Ruddick, 2010; Fan et al., 2016) and the MAG model (Morel et al. 2002a). Each of these three BOMs can simulate a wide range of water conditions and yet each is more representative of a certain water condition. The MAG model, adopted by NASA's Ocean Biology Processing Group (OBPG), has been proven to work well for clear open ocean and chlorophyll-dominated waters. We have made significant modifications to the original GSM and CCRR models to increase their ability to be representative of a wider range of water conditions. The key modifications that we made to the ocean IOP models are:

- We adopted 473 field measured hyper-spectral absorption spectra from IOCCG report 5 (IOCCG, 2006) to simulate the absorption by different types of phytoplankton, $a_{ph}(\lambda)$. Fig. 1 in the supplementary material available online shows all these spectra normalized to 443 nm.

- The the spectral slope factor S describing the logarithmic decline of detrital and Gelbstoff absorption that controls spectral shape of the absorption of detritus and Gelbstoff, $a_{dg}(\lambda)$, is not set to a fixed value, but selected randomly in the range 0.008–0.026, which is consistent with the field measurements published by Babin et al. (2003).

- The η parameter that controls the spectral shape of the particulate backscattering, $b_{bp}(\lambda)$, is not fixed, but taken from a Gaussian random distribution with a mean value of -1.0 and a standard deviation of 0.6, which is consistent with the measurements published by Reynolds et al. (2016).

- In the modified CCRR model, the γ parameter that controls the spectral shape of the attenuation of the non-algal particles (NAP), $c_{NAP}(\lambda)$, is selected randomly in the range 0.2–0.5, which is consistent with the measurements published by Babin et al. (2003).

- In the modified CCRR model, the η parameter that controls the spectral shape of the absorption of non-algal particles (NAP), $a_{NAP}(\lambda)$, is selected randomly in the range 0.005–0.02, which is consistent with the measurements published by Babin et al. (2003).

All three BOMs were used to create a comprehensive global ocean IOP dataset. The MAG model was used to simulate clear open ocean water, the modified GSM model was used to simulate moderately turbid coastal water dominated by chlorophyll, detritus and Gelbstoff, while the modified CCRR model was used to simulate highly turbid sediment-dominated water. We should emphasize that although we designated one model for different types of water, this designation does not mean that the selected BOM works well for only that type of water. In fact, each of the three ocean IOP models is capable of simulating a wide range of water conditions, and the combined ocean IOP dataset has a smooth transition from clear water to highly turbid water. A detailed description of each BOM is provided in the supplementary material available online.

2.5. Input data selection for radiative transfer simulations

To generate the large comprehensive global dataset of simulated radiances required to train the machine learning algorithms, our coupled RTM (AccuRT, Stamnes et al. (2018a)) needs input parameters that define the aerosol and water IOPs, such as aerosol optical depth (AOD), aerosol fine mode fraction (f_a), relative humidity (RH), CHL or $a_{ph}443$, $a_{dg}443$, $b_{bp}443$, TSM etc. To address the lack of a set of simultaneous measurements of aerosol and water IOPs from a variety of locations on a global scale, Fan et al. (2017) suggested using current ocean color products for this purpose, and we have adopted the same approach here to create a comprehensive global synthetic IOP dataset.

To this end we did a statistical study of the 8-day averaged 4 km spatial resolution global MODIS Aqua L3 data from the years 2011–2015. Quality control was used to ensure data quality, and pixels with negative water-leaving radiances in any wavelength channel were excluded. We randomly selected 200,000 combinations (100,000 from coastal areas and 100,000 from open ocean areas) of aerosol optical depth at 869 nm (AOT_869), chlorophyll_a concentration (CHL), absorption by chlorophyll at 443 nm (aph_443), absorption by detritus and Gelbstoff at 443 nm (adg_443) and particulate backscattering at 443 nm (bbp_443) from the L3 products over five coastal areas (East and West coast of the US, Baltic Sea and English channel, Persian Gulf and Arabian Sea, Yellow Sea, and East China Sea) and four open ocean areas (middle of North and South Pacific Ocean and the middle of North and South Atlantic Ocean). As shown in Fig. 2, the red boxes represent the selected coastal areas and the blue boxes represent the open ocean areas. The data from coastal areas were used as input to the modified GSM model and data from the open ocean areas were used as input to the MAG model. The input data for the modified CCRR model are generated from a regression model built from field measurements taken in European coastal waters (Ruddick, 2010). A total of 100,000 combinations of CHL, CDOM, and TSM were generated, and the distribution of the input data is shown in the middle panel of Fig. 3.
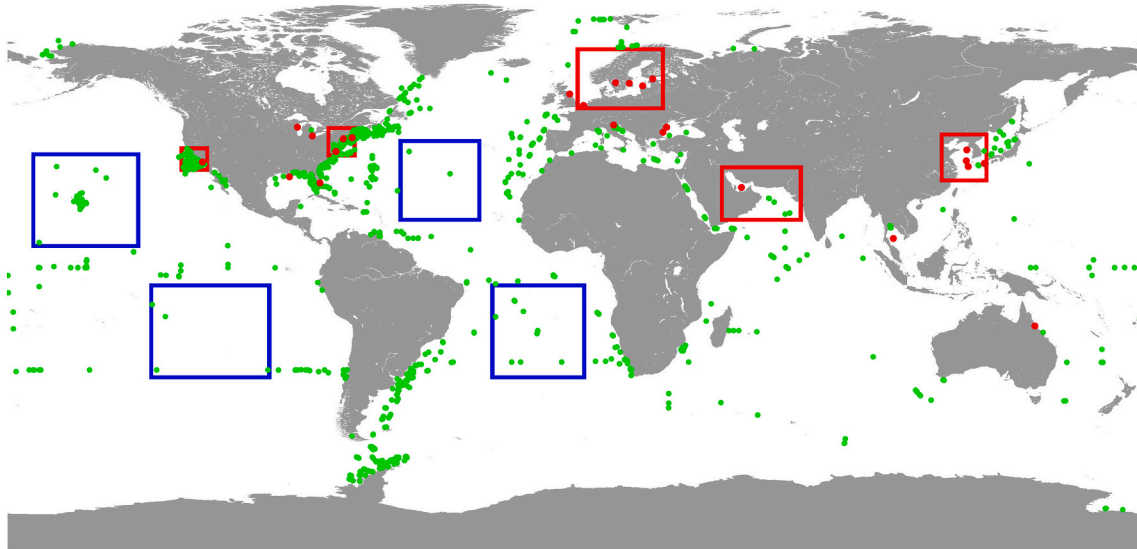
Fig. 2. Selected coastal (red boxes) and open ocean (blue boxes) areas for statistical analysis of the L3 products. The green and red dots indicate the location of in-situ measurements used for validation in Section 4, where the green dots indicates the location of MOBY and SeaBASS measurements and the red dots indicates the location of the AERONET-OC stations. (For interpretation of the references to color in this figure legend, the reader is referred to the web version of this article.)
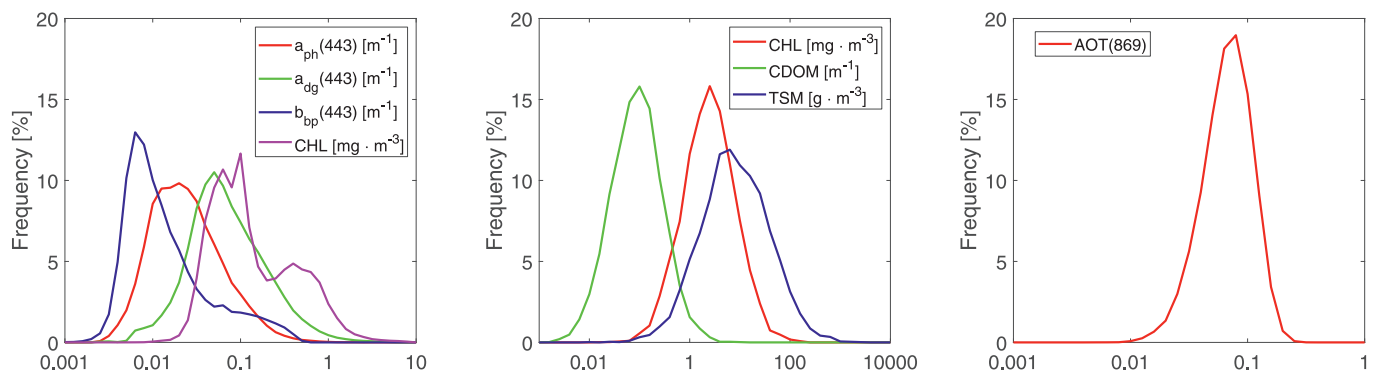

Fig. 3. Left: distribution of $a_{ph}(443)$, $a_{dg}(443)$, $b_{bp}(443)$, and CHL used in the modified GSM and MAG models. Middle: distribution of CHL, CDOM, and TSM used in the modified CCRR model (Ruddick, 2010). Right: distribution of AOD (869 nm) used in the aerosol models.

It should be emphasized that MODIS retrievals were not used for training. The few parameters we selected from the MODIS L3 data simply provided a plausible range of observed values. The other input parameters required by the RTM include atmospheric profiles, f_a, RH, the spectral chlorophyll-specific absorption coefficient $a_{CHL}^*(\lambda)$, the spectral slope factor S of CDOM or a_{dg}, the η parameter for b_{bp}, the γ and η parameters for NAP are all selected randomly from a uniform or Gaussian distribution that is consistent with published field measurements. Secondly, we used L3 data at a single wavelength each (i.e. 869 nm for AOD and 443 nm for ocean IOPs). The spectral shape of the aerosol and ocean IOPs are determined by all the other randomly selected parameters. Therefore, the spectral dependence of the aerosol or ocean IOPs we used for RT simulations differs significantly from those employed in the heritage algorithms used to obtain the L3 data. In another words, what we extracted from the L3 dataset is merely a data distribution at some reference wavelengths, as shown in the left and middle panels of Fig. 3 (i.e. for water IOPs) and the right panel (i.e. for AOT_869), which makes the RT simulations more realistic and consistent with current knowledge.

The geometry angles, i.e. solar zenith angle (θ_0), sensor zenith angle (θ), and relative azimuth angle ($\Delta\phi$), are also selected randomly from a uniform distribution. In our previous study Fan et al. (2017), we selected one set of $\{\theta_0, \theta, \Delta\phi\}$ angles for each combination of atmosphere-

aerosol-ocean IOPs in our RT simulations and generated a training dataset consisting of 100,000 simulated TOA and water-leaving radiance values. The MLNNs trained by this dataset worked well for MODIS over coastal areas. However, for a global application, we have incorporated two more ocean IOP models to simulate IOPs for open ocean and extremely turbid waters, which significantly increased the variety of the ocean IOPs. Hence, one set of geometry angles for each combination of atmosphere-aerosol-ocean IOPs is not sufficient to represent the angular distribution of the light field at the TOA and at the ocean surface. Therefore, in addition to the set $\{\theta_0 = 0, \theta = 0, \Delta\phi = 0\}$ that was used to compute the normalized water-leaving radiance:

• first, we randomly selected one θ_0 value in the range [0°, 75°] for each combination of atmosphere-aerosol-ocean IOPs;
• then the viewing angle θ was evenly divided into 7 sub-intervals in the range [0°, 70°] (i.e. [0°, 10°], [10°, 20°] ⋯ [60°, 70°]) and we randomly selected 7 viewing angles θ, one from each sub-interval;
• finally, the azimuth difference $\Delta\phi$ was evenly divided into 6 sub-intervals in the range [0°, 180°] (i.e. [0°, 30°], [30°, 60°] ⋯ [150°, 180°]) and for each selected θ angle, we randomly selected 6 $\Delta\phi$ values, one from each sub-interval.

As a result, a total of 43 geometry angles were selected for each

combination of atmosphere-aerosol-ocean IOPs. Then, a dataset consisting of a total number of $3 \times (7 \times 6 + 1) \times 100{,}000 = 12{,}900{,}000$ simulated TOA and water-leaving radiance values was created to train the MLNNs for the global AC algorithm. The increased number of geometry angles significantly increased the stability and robustness of the trained MLNN, because the 43 geometry angles represent the bidirectional reflectance distribution function (BRDF) of the atmosphere or ocean reasonably well, which significantly increased the information content that the MLNN can learn. Our RTM for the coupled atmosphere-ocean system (Stamnes et al., 2018a) has the ability to provide output for all geometry angles at once for each input of atmosphere-aerosol-ocean IOPs. Therefore, the increase of time needed to run the RT simulations is negligible.

2.6. Training of the multilayer neural networks

The multilayer neural network (MLNN) or multilayer perceptron (MLP) is a feedforward artificial neural network that can be used as a universal function approximator (Cybenko, 1989). In our case, the MLNN is used to link Rayleigh-corrected TOA radiances (L_{rc}) with normalized remote sensing reflectances ($R_{rs} = nL_w/E_d^{0+}$, where nL_w is the normalized water-leaving radiance and E_d^{0+} is the downward irradiance just above the ocean surface). A separate MLNN is used to link L_{rc} values directly to aerosol optical depths (AODs). The MLNN learns how to relate spectral L_{rc} and R_{rs} (or AOD) values from a RT simulation dataset through a supervised learning (also called training) process by minimizing the difference, also known as the cost function, between the prediction of the MLNN and the RT simulation.

Neural network training algorithms are available in many machine learning packages, such as MATLAB (2018), Scikit-Learn (Pedregosa et al., 2011), TensorFlow (Abadi et al., 2015) and others. We used the publicly available greatest descent algorithm (GDA) in Scikit-Learn, which employs an adaptive learning rate (Amari et al., 2000) to reduce the training time. However, for the same neural network structure, the precision of the GDA is slightly inferior to that of the Levenberg-Marquardt (LM) algorithm that was used to train the MLNN for MODIS with a $50 \times 25 \times 15$ structure by Fan et al. (2017). With the GDA we had to increase the number of neurons in each layer to reach the same accuracy. In addition, the new global training dataset also significantly increased the diversity of the training data, which requires larger neural networks to achieve acceptable performance. Therefore, for the global AC algorithm, we redesigned the structure of the AOD MLNN and the R_{rs} MLNN with 100, 75, and 50 neurons in the hidden layers. The size of the new MLNNs is much larger than those developed for coastal waters only by Fan et al. (2017), but it is still relatively small compared to the size of the training dataset. Therefore, it is very unlikely to lead to over-fitting. In addition, we also used L2 regularization (Neumaier, 1998) and an early stopping technique (Prechelt, 1997) in the training process to minimize the possibility of over-fitting.

In addition to the AOD and R_{rs} MLNNs described by Fan et al. (2017), we also trained an auto-associative neural network (aaNN) to identify pixels that are out of the scope of our training dataset. The inputs to the aaNN are sun-sensor geometry angles, relative humidity (RH) and spectral L_{rc} values (e.g. there are 13 inputs for MODIS, 3 geometry angles, 1 RH value, and 9 spectral bands), and the output of the aaNN is the spectral L_{rc} values. After being trained by the same training dataset, the aaNN works as a duplicator. If the input data are within the range of the training dataset and the shape of the spectral L_{rc} is very close to that of the training dataset, then the aaNN output will duplicate the input spectral L_{rc} with a very high precision. But if some of the input data are out of the range or the shape of the spectral L_{rc} is not included in the training dataset, then the output from the aaNN deviates significantly from the input spectral L_{rc}, i.e. the band-averaged percentage difference is larger than 5%. Therefore, by comparing the output from aaNN with the input spectral L_{rc}, we can identify pixels that are out of scope of the training dataset. This capability of the aaNN is due to the bottleneck

layer in the neural network structure.

The aaNN also has 3 hidden layers. The number of neurons in the first and third layers is set to equal the number of inputs. The second layer is the bottleneck layer with a much smaller number of neurons, and designed such that a well trained aaNN is able to duplicate only input data available in the training dataset. For our purpose, we have found that setting the number of neurons in the bottleneck layer equal to half of the number of neurons in the input layer works well for identifying pixels with out of scope radiances. This structure (e.g. for MODIS the aaNN structure is $13 \times 7 \times 13$) ensures that 99.5% of the data in the training dataset can be duplicated by the trained aaNN with very high precision (i.e. band-averaged deviation less than 0.1%).

2.7. Global Ocean IOP retrieval algorithms

The spectral behavior of the remote sensing reflectance, R_{rs}, is primarily determined by the water IOPs, i.e. absorption by phytoplankton ($a_{ph}(\lambda)$), absorption by detritus and Gelbstoff ($a_{dg}(\lambda)$), and particulate backscattering ($b_{bp}(\lambda)$). Therefore, the water IOPs can be inferred from spectral R_{rs} data. Semi-analytical models (Lee et al., 2002; IOCCG, 2006; Smyth et al., 2006) are frequently used to infer water IOPs from R_{rs} data. These semi-analytical models are based on empirical relations linking R_{rs} data with water IOPs (IOCCG, 2006):

$$R_{rs}(\lambda) = G(\lambda)\left(\frac{b_b(\lambda)}{a(\lambda) + b_b(\lambda)}\right) \tag{4}$$

Here $b_b(\lambda)$ and $a(\lambda)$ are the water backscattering and absorption coefficients, respectively. The function $G(\lambda)$ is approximated by a polynomial with coefficients derived by fitting RT simulations or field measurements. However, due to the complexity of the water body, especially in coastal/inland water areas, several agents that scatter and absorb radiation (i.e. different types of algae, detritus, Gelbstoff, etc.) are present in the water body and they do not co-vary with each other. Hence, each contributes to the R_{rs} data independently. The empirical approach may be a good approximation in clear (open ocean) water areas, but as the water body becomes more complex in coastal and inland water areas, this simple equation is inadequate to represent the relation between R_{rs} data and water IOPs. Instead, a coupled atmosphere-ocean RTM (such as AccuRT Stamnes et al. (2018a)) was used here to accurately link R_{rs} data with water IOPs.

As a default ocean IOP algorithm in NASA's SeaDAS software package, the GIOP algorithm (Werdell et al., 2013) is designed as a general framework for relating the spectral distribution of $R_{rs}(\lambda)$ to the ocean IOPs. However, in order to determine the function $G(\lambda)$, the GIOP algorithm relies on $R_{rs}(\lambda)$ values derived from an approximate f/Q method to deal with bidirectional effects, and the eigenvectors (i.e. the spectral shape) for $a_{ph}(\lambda)$, $a_{dg}(\lambda)$, and $b_{bp}(\lambda)$ are fixed in the default configuration of the algorithm. Although the GIOP algorithm provides the option to input a set of user defined eigenvectors, it still requires a priori knowledge from the user to select the eigenvectors. This requirement is not suitable for operational use.

Machine learning algorithms have also been proposed to retrieve water IOPs from R_{rs} data, and some use neural networks to improve the estimation of the function $G(\lambda)$ in Eq. (4) (Chen et al., 2014; Li et al., 2019). Ioannou et al. (2011) proposed a neural network algorithm to derive total absorption (a) and total backscattering (b_b) coefficients in addition to a_{ph} and a_{dg}. However, the algorithm was designed to retrieve water IOPs only at 442 nm and its application to satellite ocean color sensor retrievals was not validated.

In contrast, our comprehensive global synthetic dataset provides an accurate link between R_{rs} data and water IOPs. Our input dataset includes a variety of different water IOPs (300,000 cases to be exact) generated from several water BOMs (see Section 2.4), and is therefore expected to be representative of most realistic water conditions. To infer water IOPs from R_{rs} data, we propose a more direct approach. We again

Table 1
Details of the 11 sensors supported by OC-SMART.

Sensor	Spectral Bands[a] [nm]	Resolution	Level 1B/1C Data Source
SeaStar/ SeaWiFS	412, 443, 490, 510, 555, 670, 765, 865	1 km	NASA OBPG OceanColor Website[b]
Aqua/ MODIS	412, 443, 488, 531, 547, 667, 678, 748, 869	1 km	NASA LAADS DAAC
SNPP/VIIRS	410, 443, 486, 551, 671, 745, 862	750 m	NASA LAADS DAAC
ISS/HICO	78 bands[c] in 400–900 nm with 5.7 nm spectral resolution	90 m	NASA OBPG OceanColor Website
Landsat8/ OLI	443, 482, 561, 665, 865	30 m	U.S. Geological Survey(USGS) archives
DSCOVR/ EPIC	388, 443, 551, 680, 779, 865	10 km	NASA ASDC DAAC
Sentinel-2A/ MSI	443, 492, 560, 665, 704, 740, 783, 835, 865	60 m[d]	ESA Copernicus Open Access
Sentinel-2B/ MSI	442, 492, 559, 665, 704, 739, 780, 835, 864	60 m[d]	ESA Copernicus Open Access
Sentinel-3/ OLCI	400, 412, 443, 490, 510, 560, 620, 665, 674, 681, 709, 754, 779, 865, 885	300 m	ESA Copernicus Open Access
GCOM-C/ SGLI	380, 412, 443, 490, 530, 565, 672, 763, 867	1 km	JAXA Globe Portal System
COMS/GOCI	412, 443, 490, 555, 660, 680, 745, 865	500 m	Korean Ocean Satellite Center (KOSC)
FengYun-3D/MERSI	412, 443, 490, 555, 670, 709, 746, 865	1 km	FengYun Satellite Data Center

[a] Only the spectral bands required by OC-SMART are listed.

[b] NASA's OBPG OceanColor Website provides SeaWiFS level 1A data, which need to be processed by NASA's SeaDAS software to generate level 1B data.

[c] Spectral bands that are strongly affected by water vapor and oxygen absorption (i.e. around 725, 765 and 825 nm) were excluded.

[d] All bands aggregated to 60 m spatial resolution.

employ machine learning techniques to directly infer 3 spectral water IOPs (i.e. $a_{\mathrm{ph}}(\lambda)$, $a_{\mathrm{dg}}(\lambda)$ and $b_{\mathrm{bp}}(\lambda)$) from the satellite retrieved spectral R_{rs} data, at the same set of wavelengths as the input R_{rs} data up to 700 nm (see Table 1 for details). To ensure a smooth transition between different water types, a single multilayer neural network (MLNN) is preferred for each water IOP. Therefore, three separate MLNNs (i.e. aph_MLNN, adg_MLNN and bbp_MLNN) were trained from the simulated dataset and each will retrieve the corresponding spectral water IOP from the spectral $R_{\mathrm{rs}}(\lambda)$ data retrieved by the $R_{\mathrm{rs}}(\lambda)$ MLNN as discussed in Section 2.6. These machine learning based water IOP algorithms have been validated against field measurements using SeaWiFS data and they show significant improvement when compared with the GIOP algorithm, as demonstrated in Section 4.2.

3. Ocean color - simultaneous marine and aerosol retrieval tool

The machine learning based AC and ocean IOP retrieval algorithms are implemented in our multi-sensor data analysis platform, Ocean Color - Simultaneous Marine and Aerosol Retrieval Tool (OC-SMART). Currently OC-SMART supports ocean color data retrievals from 11 multi-spectral and hyper-sepctral sensors onboard satellites operated by the National Aeronautics and Space Administration (NASA), the National Oceanic and Atmospheric Administration (NOAA), the European Space Agency (ESA), the Japan Aerospace Exploration Agency (JAXA), the Korea Institute of Ocean Science and Technology (KIOST), and the China Meteorological Administration (CMA), which include: SeaStar/ SeaWiFS, MODIS/Aqua, SNPP/VIIRS, ISS/HICO, Landsat8/OLI, DSCOVR/EPIC, Sentinel-2/MSI, Sentinel-3/OLCI, GCOM-C/SGLI, COMS/GOCI and FengYun-3D/MERSI. Some characteristics of the supported sensors are provided in Table 1. The machine learning based AC

algorithm implemented in OC-SMART is applicable to any combination of suitable spectral bands. Hence, OC-SMART can easily be modified to support future satellite missions, such as the Plankton, Aerosol, Cloud, ocean Ecosystem (PACE) mission.

A flowchart of the satellite image processing chain in OC-SMART is shown in Fig. 4. The processing described in the following sections were applied to satellite images obtained by the sensors supported by OC-SMART.

3.1. Land/water mask

Each pixel in a satellite image was first classified as land or water based on the geolocation (i.e. latitude and longitude). If the land/water mask is provided with the level 1b data, such as for Sentinel-3/OLCI and GCOM-C/SGLI, then these land/water masks were used in OC-SMART. If the land/water mask was not included in the sensor level 1b data, OC-SMART will run a land/water classification algorithm implemented in the code. Several land/water databases were implemented in OC-SMART. The Global Self-consistent, Hierarchical, High-resolution Geography (GSHHG) database (Wessel and Smith, 1996) was used to classify land and water pixels for sensors with lower spatial resolution, i. e. footprint size less than 200 m at nadir direction, and the Global Surface Water (GSW) database (Pekel et al., 2016) was used for high spatial resolution sensors, such as Landsat8/OLI, Sentinel-2/MSI and ISS/HICO. COMS/GOCI is onboard a geostationary satellite. Therefore, a land/water database generated by the Korea Ocean Satellite Center (KOSC) was used to classify land and water pixels for GOCI images.

3.2. Conversion of TOA radiance to reflectance

The satellite-measured radiance L was converted to a bidirectional reflectance distribution function (BRDF) defined by: $\rho = L/(F_0 \cdot \mu_0)$ in units sr^{-1} where F_0 is the solar irradiance and μ_0 is the cosine of the solar zenith angle. This definition is different from the conventional use of a dimensionless bidirectional reflection factor (BRF) defined as $\rho' = \pi \cdot L/(F_0 \cdot \mu_0)$ by a factor of π. The BRF is defined such that it yields the albedo if the radiance distribution were to be isotropic, which is far from the case for the radiation field in the Earth atmosphere-ocean system. The factor π may lead to confusion because the BRF can be larger than 1 (e.g. near the sunglint region), but integration of the cosine-weighted radiance over the entire upper hemisphere accurately yields the reflected energy.

3.3. Vicarious calibration of TOA reflectance

The purpose of the vicarious calibration is to reduce the systematic bias in the retrieved water-leaving radiance (L_w) when compared with high quality in-situ measurements. A set of vicarious gain factors (also called g-factors) were applied to the TOA reflectance in addition to the sensor radiometric calibration. The derivation of the g-factors is described in some detail in several papers (Franz et al., 2007; Werdell et al., 2007; Bailey et al., 2008; Mélin and Zibordi, 2010). The g-factors generally have a difference smaller than 1% when derived from different in-situ data sources (eg. MOBY, NOMAD, AERONET-OC etc.). Therefore, in the current version of OC-SMART, the g-factors were set to be unity (i. e. 1.0) or if available, to the ones derived for heritage algorithms, such as the ones implemented in NASA's SeaDAS platform. Although the g-factors derived for the heritage algorithms may be imperfect when applied to OC-SMART, we have found that they can indeed help reduce systematic bias in L_w retrievals. A dedicated vicarious calibration designed for the neural network approach adopted in OC-SMART will be developed and implemented in future versions.

3.4. Correction for atmospheric gas transmittance

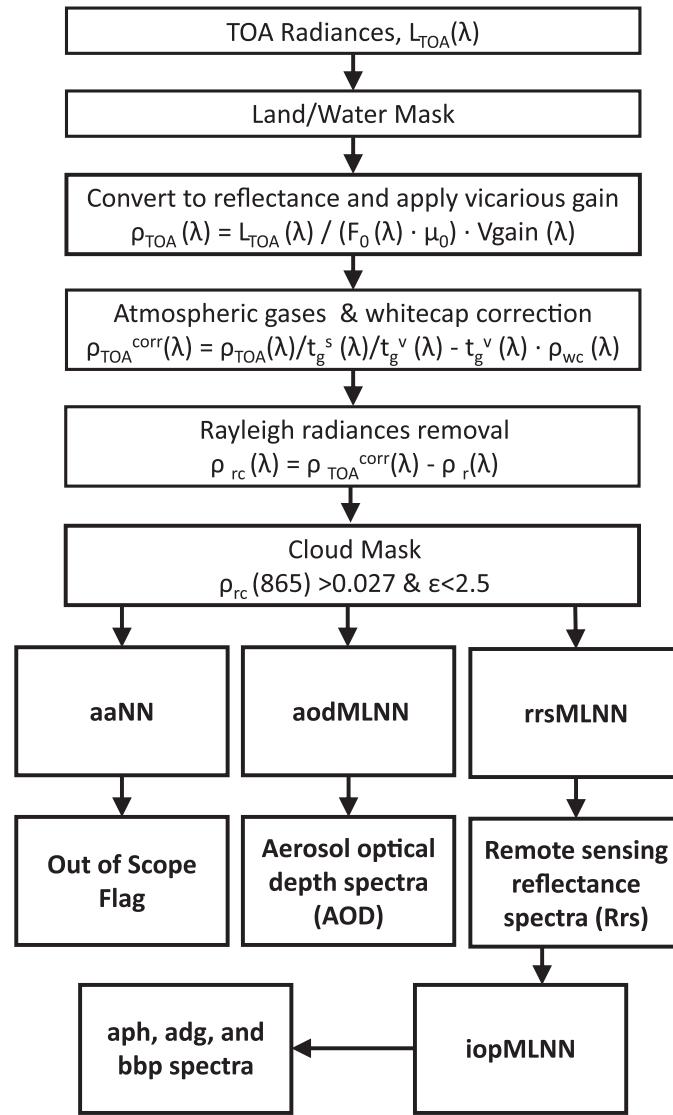Most of the spectral bands used to derive ocean color products are

Fig. 4. Flow chart of the OC-SMART satellite image processing chain. F_0 is the solar irradiance corrected for Earth-sun distance, μ_0 is the cosine of the solar zenith angle, *Vgain* is the vicarious calibration factor, t_g^s and t_g^v are the downward and upward diffuse transmittances, ρ_{wc} is the whitecap reflectance, ρ_r is the Rayleigh reflectance corrected for real time sea surface wind speed and sea surface pressure and $\varepsilon = \frac{max(\rho(412),\rho(555),\rho(670),\rho(865))}{min(\rho(412),\rho(555),\rho(670),\rho(865))}$.

located in atmospheric window regions where the impact of atmospheric gas absorption is minimal. However, in the UV and visible spectral range, ozone has a continuum absorption that must be corrected. OC-SMART uses real time ozone data derived from Aura/OMI to estimate the diffuse transmittance due to ozone absorption. Nitrogen dioxide (NO_2) also accounts for some atmospheric absorption in the visible range, mainly in the blue part of the spectrum (Ahmad et al., 2007). OC-SMART currently uses climatology NO_2 data derived by the NASA Ocean Biology Processing Group (OBPG) to correct for the NO_2 transmittance. Oxygen absorption (O_2) is also taken into account in OC-SMART for sensors, such as SeaWiFS and SGLI, that have spectral bands located in the oxygen A-band (i.e. between 759 and 770 nm). The sensor relative spectral response functions are used to compute the band-averaged absorption coefficient for the atmospheric gases. The diffuse transmittance along the solar (downward) and sensor viewing (upward) directions were computed as:

$$t_g^s(\lambda) = exp[-\tau(\lambda)/cos(\theta_0)] \tag{5}$$

$$t_g^v(\lambda) = exp[-\tau(\lambda)/cos(\theta)] \tag{6}$$

where τ is the optical depth of the atmospheric gas (e.g. ozone or NO_2), θ_0 is the solar zenith angle, and θ is the sensor zenith angle. Spectral bands that are strongly affected by water vapor absorption are currently excluded by OC-SMART (e.g. 725 nm and 825 nm in HICO).

3.5. Correction of whitecap reflectance

Whitecaps consist of foam-like material formed by breaking waves at the ocean surface. Observational data show that the amount of whitecaps can be related to the wind speed (Monahan and Muircheartaigh, 1980). In OC-SMART we have adopted the method described by Stramska and Petelski (2003) to compute the fractional area covered by whitecaps and the wavelength dependence of the whitecap reflectance is adopted from Frouin et al. (1996). The near real time surface wind speed data used to estimate the whitecap fraction are obtained from the National Center for Environmental Prediction (NCEP) data archive available on NASA's OBPG Ocean Color website.

3.6. Correction of Rayleigh reflectance

The reflectance due to pure Rayleigh scattering is estimated from pre-generated look up tables (LUTs) based on geometry angles, atmospheric pressure (Wang, 2005), and surface wind speed for each pixel and then removed from the TOA reflectance after the correction for atmospheric gas absorption and whitecap reflectance. Use of the Rayleigh-corrected radiance ρ_{rc} to derive the ocean color products is not strictly necessary, and should not be used for large solar zenith angles, as discussed in Section 6.2. However, in the current version of OC-SMART, we use ρ_{rc} because it increases the sensitivity of the algorithm and allows for a clean comparison with results derived from heritage algorithms since exactly the same TOA reflectance input is used in OC-SMART as in, for example, the NASA SeaDAS platform.

3.7. Cloud mask

Cloud contaminated pixels need to be identified before the AC algorithm can be applied. The standard cloud mask algorithm (STDCM, Patt et al. (2003)) in SeaDAS for ocean color sensors is a threshold method based on use of a single NIR band (e.g. 865 nm). The pixel is classified as cloudy if $\rho_{rc}(865) > 0.027$ (Patt et al., 2003). This algorithm works quite well over open ocean areas, but it is sensitive enough to be incorrectly triggered by highly scattering turbid water, by moderately high concentrations of aerosols or by increased Rayleigh scattering at high solar zenith angles (Nordkvist et al., 2009; Banks and Mélin, 2015). A number of studies, including Wang and Shi (2006) and Nordkvist et al. (2009), have been conducted to address this issue. Banks and Mélin (2015) showed that improved cloud screening results were obtained by using the method proposed by Nordkvist et al. (2009) (N09CM). Therefore, this method is currently adopted in OC-SMART. The N09CM algorithm identifies a pixel as cloudy when $\rho_{rc}(865) > 0.027$ and $\varepsilon = \frac{max(\rho_{rc}(412),\rho_{rc}(555),\rho_{rc}(670),\rho_{rc}(865))}{min(\rho_{rc}(412),\rho_{rc}(555),\rho_{rc}(670),\rho_{rc}(865))} < 2.5$. In Section 6.3 we discuss

developments of a threshold-free, machine learning based cloud mask that will be included in upcoming versions of OC-SMART.

3.8. Sunglint correction

In OC-SMART, the sunglint is corrected using a machine learning method which is included implicitly in the training of the R_{rs} MLNN. As described in Section 2.1, in our training dataset, we have included simulation cases for 'skyglint' and 'moderate' sunglint. Therefore, the trained MLNN has learned to deal with sunglint and appears to be capable of retrieving accurate ocean color products from moderate sunglint areas, although a more comprehensive study is needed to assess the performance of OC-SMART in the presence of sunglint. Strong sunglint will trigger the N09CM cloud mask algorithm to mask the pixel as cloud. Therefore, OC-SMART does not utilize a specific sunglint algorithm, but relies on the cloud mask algorithm to identify areas with strong sunglint. Fig. 5 shows one example of CHL retrievals from a Sentinel-3/OLCI image with strong sunglint contamination obtained on April 3, 2017. The purple color in panel (c) shows the strong sunglint area that was masked by NASA's SeaDAS sunglint algorithm. The retrieval from OC-SMART, i.e. panel (b), shows no residue of the sunglint pattern in the weak to moderate sunglint areas. However, areas with strong sunglint, i.e. the white areas in panel (b), masked as cloud by the N09CM cloud mask algorithm, are unretrievable by OC-SMART.

3.9. Application of the machine learning algorithms

After carrying out the pixel identification and pre-processing described in the previous sections, one may input the ρ_{rc} spectra, solar-sensor geometry angles and some ancillary data (e.g. relative humidity) to the trained R_{rs} MLNN and AOD MLNN to derive the spectral normalized R_{rs} values up to 800 nm and spectral AOD values up to 900 nm. Then the retrieved spectral normalized R_{rs} values are input to the ocean IOP MLNNs (i.e. aph_MLNN, adg_MLNN and bbp_MLNN, see

CHLa *[mg/m^3]*
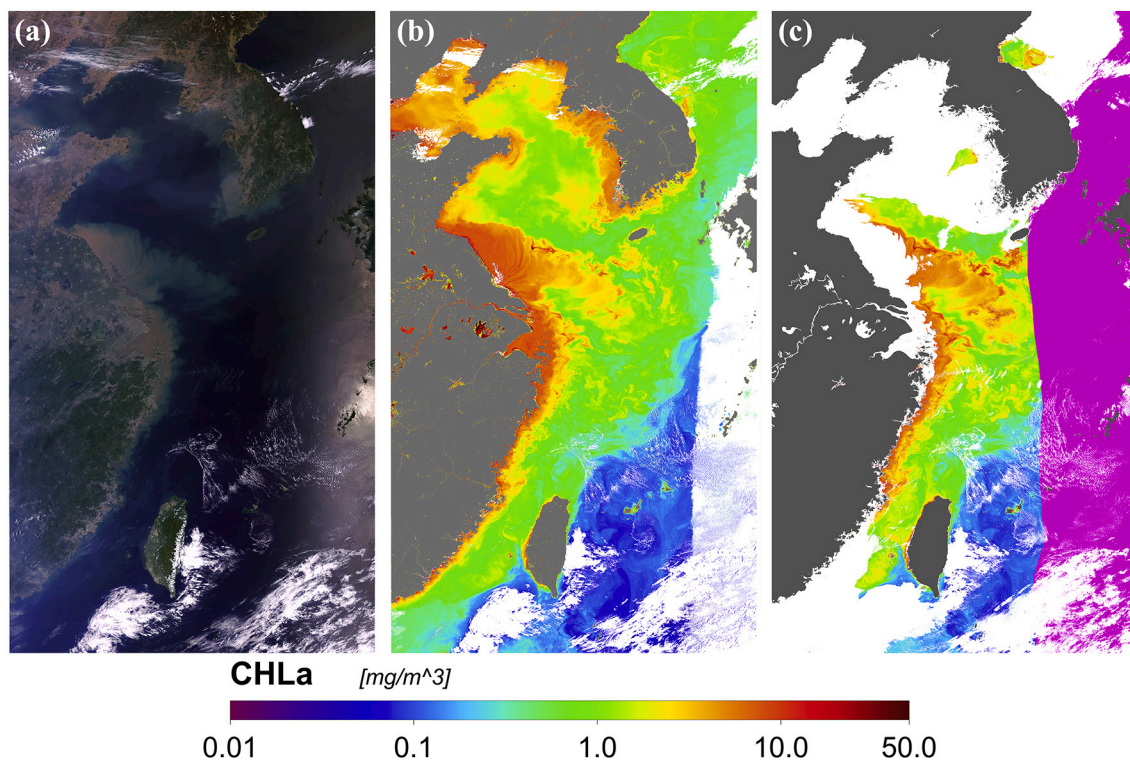
0.01   0.1   1.0   10.0   50.0

Fig. 5. Comparison of CHL retrievals from a OLCI image obtained on April 3, 2017. (a) OLCI RGB image; (b) CHL retrieved by OC-SMART; (c) CHL retrieved by NASA SeaDAS. The purple color in (c) indicates the area contaminated with strong sunglint, and white color in panels (b) and (c) indicates cloud mask results. (For interpretation of the references to color in this figure legend, the reader is referred to the web version of this article.)

Section 2.7) to retrieve spectral water IOPs up to 700 nm, including $a_{ph}(\lambda)$, $a_{dg}(\lambda)$, and $b_{bp}(\lambda)$. A trained auto associative neural network (aaNN) is used to identify pixels that are out of the scope of the training dataset and establish quality flags. The input and output parameters for each MLNN are listed below:

1. aaNN

- Input: $\cos(\theta_0)$, $\cos(\theta)$, $\cos(\Delta\phi)$, $\log_{10}[\rho_{rc}(\lambda_i)]$, $\log_{10}(RH)$.
- Output: $\rho_{rc}(\lambda_i)$ and out of scope quality flags.

2. AOD MLNN

- Input: $\cos(\theta_0)$, $\cos(\theta)$, $\cos(\Delta\phi)$, $\log_{10}[\rho_{rc}(\lambda_i)]$, $\log_{10}(RH)$.
- Output: $AOD(\lambda_i)$.

3. R_{rs} MLNN

- Input: $\cos(\theta_0)$, $\cos(\theta)$, $\cos(\Delta\phi)$, $\log_{10}[\rho_{rc}(\lambda_i)]$.
- Output: normalized $R_{rs}(\lambda_{rrs})$.

4. a_{ph} MLNN, a_{dg} MLNN and b_{bp} MLNN

- Input: normalized $R_{rs}(\lambda_{rrs})$.
- Output: $a_{ph}(\lambda_{iop})$, $a_{dg}(\lambda_{iop})$ and $b_{bp}(\lambda_{iop})$.

Note that λ_i denotes the spectral bands listed in Table 1, and λ_{rrs} denotes spectral bands at wavelengths shorter than 800 nm. The R_{rs} retrievals at wavelengths longer than 800 nm have relatively larger errors and are therefore excluded. λ_{iop} denotes spectral bands at wavelengths shorter than 700 nm due to limitations in the field measurements used to construct the ocean IOP models, i.e. the measured chlorophyll absorption data are available only for wavelengths shorter than 700 nm. The out of scope pixels are flagged by calculating the mean percentage difference between the input $\rho_{rc}(\lambda_i)$ and the aaNN output. If the mean percentage difference is larger than 6%, the pixel is flagged as out of scope. The 6% criterion is based on the 3-sigma rule of the noise level (i.e. 2%) that we added to the TOA reflectance in the training dataset.

3.10. Correction for bidirectional effects in remote sensing reflectance

The water-leaving radiance (L_w) and remote sensing reflectance (R_{rs}) is anisotropic due primarily to the asymmetry of the scattering phase function of the particles embedded in the water. The ocean color sensors on board remote sensing satellite platforms take measurement at a specific sun-sensor geometry. Therefore, bidirectional effects must be accounted for in order to derive the normalized remote sensing reflectance, nR_{rs}, which is used in many ocean color algorithms to derive in-water constituents. The heritage algorithms employ the method adopted by OBPG (Morel et al. 2002b), denoted as the *f/Q* method, which works well in open ocean areas, but is less accurate in complex coastal waters (Voss et al., 2007; Gleason et al., 2012; Fan et al., 2016). With a coupled atmosphere-ocean RT model, the normalized nR_{rs} can be computed accurately, without using the approximate *f/Q* method as reported previously (Fan et al., 2016, 2017). Our coupled atmosphere-ocean RTM (AccuRT, Stamnes et al. (2018a)) produces R_{rs} values at randomly selected sun-sensor geometry angles as well as in the nadir direction as explained in Section 2.5, and we trained the R_{rs} MLNN to derive normalized nR_{rs} values directly from the ρ_{rc} values. Therefore, bidirectional effects are implicitly taken into account in the derived R_{rs} values. Hence, there is no need for any explicit BRDF correction.

4. Results – Validation and application of OC-SMART

The performance of OC-SMART is first tested using an independent synthetic testing dataset. Then the ocean color products retrieved by OC-

Table 2

Details of the AERONET–OC stations: location, time period selected for validation, and number of match-up data used.

Station	Location	Time Period	Number of Match-ups
Abu_Al_Bukhoosh	25.495 N, 53.146E	2004–2008	45
ARIAKE_TOWER	33.104 N, 130.272E	2018	26
Blyth_NOAH	55.146 N, 1.421 W	2016–2017	2
COVE_SEAPRISM	36.900 N, 75.710 W	2006–2015	111
Gageocho_Station	33.942 N, 124.593E	2011–2012	28
Galata_Platform	43.045 N, 28.193E	2014–2018	741
Gloria	44.600 N, 29.360E	2011–2018	919
GOT_Seaprism	9.286 N, 101.412E	2012–2016	23
Gustav_Dalen_Tower	58.594 N, 17.467E	2005–2018	761
Helsinki_Lighthouse	59.949 N, 24.926E	2006–2017	941
Ieodo_Station	32.123 N, 125.182E	2013–2018	63
Irbe_Lighthouse	57.751 N, 21.723E	2018	6
Lake_Erie	41.826 N, 83.194 W	2016–2018	32
Lake_Okeechobee	26.902 N, 80.789 W	2018	18
LISCO	40.955 N, 73.342 W	2009–2018	198
Lucinda	18.520S, 146.386E	2010–2018	143
MVCO	41.300 N, 70.567 W	2004–2018	798
Palgrunden	58.755 N, 13.152E	2008–2018	492
Socheongcho	7.423 N, 124.738E	2016–2018	171
South_Greenbay	44.596 N, 87.951 W	2018	22
Thornton_C-power	51.533 N, 2.955E	2015–2018	205
USC_SEAPRISM	33.564 N, 118.118 W	2012–2018	863
Venice	45.314 N, 12.508E	2001–2018	2897
WaveCIS	28.867 N, 90.483 W	2010–2018	675
Zeebrugge	51.362 N, 3.120E	2014	15

SMART have been validated against in-situ measurements from MOBY (Clark et al., 2003), SeaBASS (Werdell et al., 2002), and AERONET-OC (Zibordi et al., 2009) for several sensors. Table 2 shows the details of the AERONET-OC stations used for validation. For SeaWiFS, MODIS, and VIIRS, we used the validation dataset processed by NASA OBPG (Bailey and Werdell, 2006), which includes in-situ R_{rs} data from MOBY, SeaBASS, and AERONET-OC, and in-situ ocean IOP data (i.e. a_{ph}, a_{dg}, and b_{bp}) from the SeaBASS database. These in-situ data are also used for the validation of NASA's SeaDAS products. Therefore, a comparison with NASA SeaDAS results will be presented. For Sentinel-3/OLCI, Sentinel-2/MSI, and Landsat8/OLI, the validation is performed on in-situ measurements from AERONET-OC stations. The satellite retrieval extraction and quality control protocols generally follow those recommended by Bailey and Werdell (2006), which are also described in the supplementary material available online. A linear interpolation algorithm was applied to the in-situ measurements to account for the wavelength difference with satellite sensors. The validation for COMS/GOCI, presented in Section 4.3, was performed against field measurements made both by Korea Institute of Ocean Science and Technology (KIOST) and against data obtained at the three AERONET-OC stations within the field of view of the GOCI sensor. The performance of the OC-SMART algorithms was assessed using the coefficient of determination (R^2), the average percentage difference (APD), the mean percentage bias, root-mean-square difference (RMSD), and the slope of the linear regression between in-situ data and satellite retrievals, which are defined as:

$$R^2 = \left[\frac{1}{N} \sum_{i=1}^{N} \left(\frac{X_i - \overline{X}}{\sigma_X} \right) \left(\frac{Y_i - \overline{Y}}{\sigma_Y} \right) \right]^2 \tag{7}$$

$$APD \ [\%] = \frac{1}{N} \sum_{i=1}^{N} \left| \frac{X_i - Y_i}{Y_i} \right| \times 100 \tag{8}$$

$$Bias \ [\%] = \frac{1}{N} \sum_{i=1}^{N} \frac{X_i - Y_i}{Y_i} \times 100 \tag{9}$$

$$RMSD = \sqrt{\frac{\sum_{i=1}^{N}(X_i - Y_i)^2}{N}} \tag{10}$$

where X is the value of AOD or R_{rs} or ocean IOPs retrieved by the algorithms, Y is the corresponding in-situ measurement value, and σ_X and σ_Y are the standard deviations.

4.1. Validation of OC-SMART R_{rs} retrievals

The green and red dots in Fig. 2 show the location of the in-situ measurements used to validate the R_{rs} products retrieved from SeaWiFS (1997–2010), MODIS on Aqua (2002–2017), and VIIRS SNPP (2012–2017) images. The green dots show the location of MOBY and SeaBASS measurements and the red dots show the location of AERONET-OC stations. It is clear that the validation dataset covers global water conditions including open ocean, coastal water, and inland lakes. VIIRS images are available for only a short period of time. Therefore, the in-situ measurements used to validate VIIRS retrievals are mostly from MOBY and AERONET-OC stations. Figs. 6–8 show the validation results processed by OC-SMART and NASA SeaDAS v7.5.2 default algorithms against SeaWiFS, MODIS on Aqua, and VIIRS images, respectively, and N indicates the number of validation data available for each band. It is clear that OC-SMART performs well for the entire global validation dataset for all the three sensors.

One clear advantage of OC-SMART is the complete resolution of the negative R_{rs} issue that persists in the heritage algorithms, especially in blue and red bands. Detailed validation results are shown in Tables S1-S3 (see supplementary material available online). Compared with in-situ measurements, the R_{rs} retrievals obtained by OC-SMART are generally better than those obtained by SeaDAS, especially in blue and red bands. OC-SMART R_{rs} retrievals have higher R^2 and lower APD and RMSD in almost all the bands, implying that the OC-SMART R_{rs} retrievals have better correlation with the in-situ measurements and smaller differences. For SeaWiFS, OC-SMART reduced the APD by up to 25% at 412 nm, up to 18% in 670 nm, and about 2–5% in the other bands when compared with SeaDAS results. For MODIS, OC-SMART retrievals are comparable with SeaDAS in the 443–547 nm spectral range, but still reduced the APD by 7% at 412 nm and 667 nm, and by 11% at 678 nm. For VIIRS, OC-SMART reduced APD by 26% at 410 nm and 3–7% in other bands.

The higher APD in SeaDAS retrievals at blue and red bands are generally due to the negative values in the retrievals. Despite the fact that the match-up satellite images have passed the quality control procedure, there are up to 10% of negative R_{rs} values in the blue band and up to 5% in the red bands in SeaDAS retrievals. The mean bias in SeaDAS retrievals is generally lower than for OC-SMART in the blue bands. However, this result is also due to the existence of negative values and therefore may not reflect the true performance of the SeaDAS algorithm. The slope of the linear regression between the in-situ data and the retrievals from both algorithms also shows the deviation from the 1:1 line, which indicates a certain bias introduced by the algorithm. For OC-SMART, one reason for this deviation could be the imperfect g-factors used for vicarious calibration and we expect the bias to be reduced once we finalize the derivation of the g-factors. Another possible reason is that the ocean IOP models may not perfectly represent the type of water in the real world, implying that a certain bias may still exist in the training dataset. This bias may be reduced by filtering the training dataset using the distribution extracted from the in-situ data.

The validation of the R_{rs} retrievals for Sentinel-3/OLCI, Sentinel-2A&B/MSI, and Landsat-8/OLI (Pahlevan et al., 2014) was performed using in-situ measurements from AERONET-OC stations, including Galata, Gloria, Gustav Dalen Tower, Helsinki Lighthouse, Ieodo, LISCO, Lucinda, MVCO, Palgrunden, Socheongcho, USC SEAPRISM, AAOT, and WaveCIS. Version 3 level 2.0 quality assured data were used for the validation. The extraction and quality control of the satellite retrievals generally followed recommendations provided by Bailey and Werdell (2006). However, the spatial resolution of these 3 sensors is relatively high (see Table 1). Therefore, to minimize the impact from the AERONET-OC stations (i.e. shadowing, higher reflectance from the physical structure of the stations, etc.), we modified the data extraction procedure as follows: for OLCI, the center pixel from the 3×3 box is excluded, and for MSI and OLI, the center 9 pixels (3×3) from the 5×5 boxes are excluded. The detailed validation results are provided in Tables S4-S6 (see supplementary material available online). In general, the validation shows a good agreement between the OC-SMART retrievals and the in-situ measurements and the performance of OC-SMART for OLCI, MSI, and OLI is consistent with the application to SeaWiFS, MODIS, and VIIRS, which are validated using a global ocean dataset. The relatively larger APD at 400 nm for OLCI is partially due to the linear extrapolation of the AERONET-OC measurement data. The relatively lower performance for Sentinel-2A&B/MSI and Landsat-8/OLI
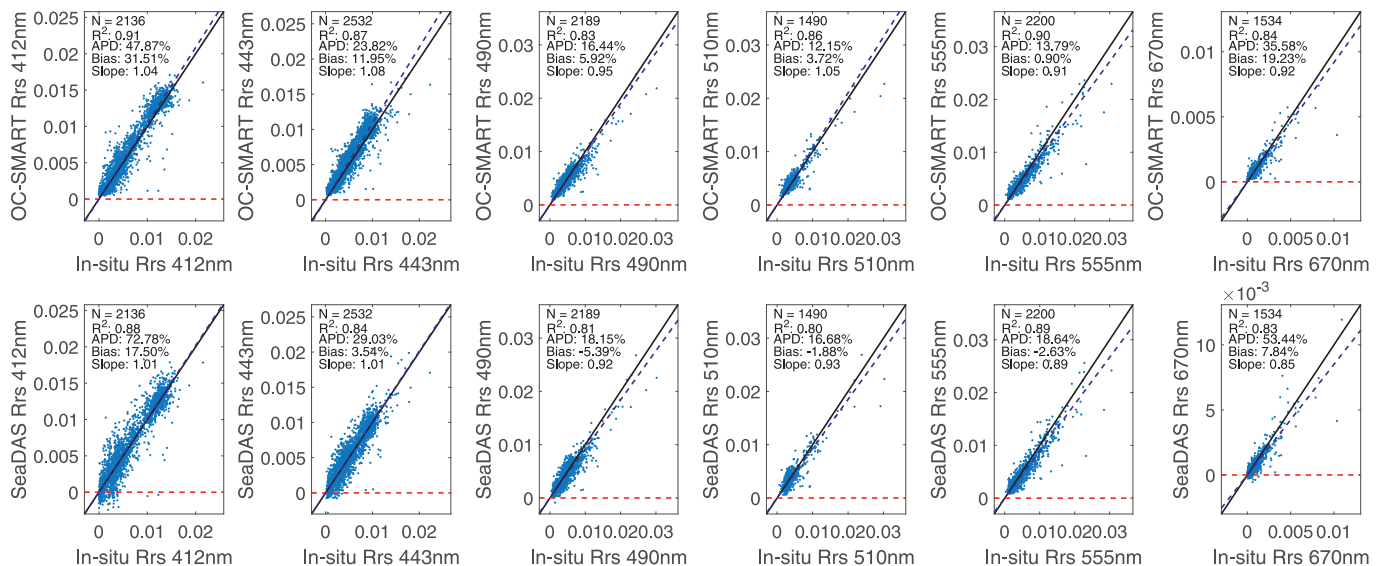

Fig. 6. Validation of R_{rs} retrievals from SeaWiFS images against in-situ measurements. Top: retrieval by OC-SMART, bottom: retrieval by NASA SeaDAS v7.5.2. Data below the red dashed line are negative values. The blue dashed line shows linear regression. (For interpretation of the references to color in this figure legend, the reader is referred to the web version of this article.)
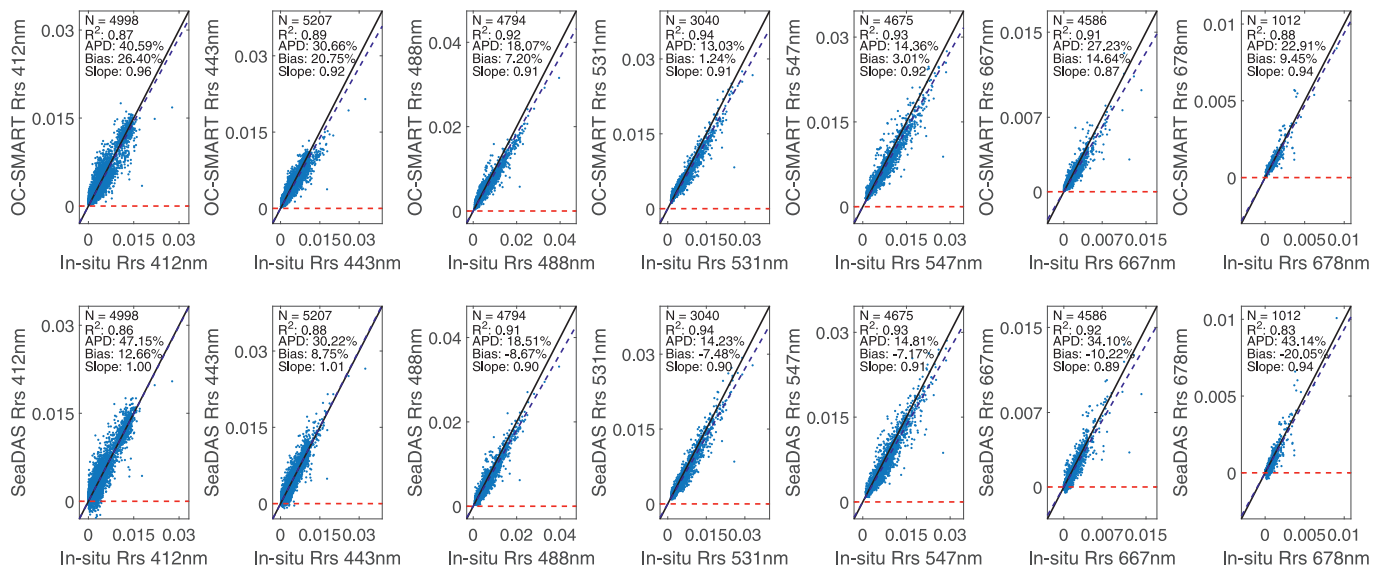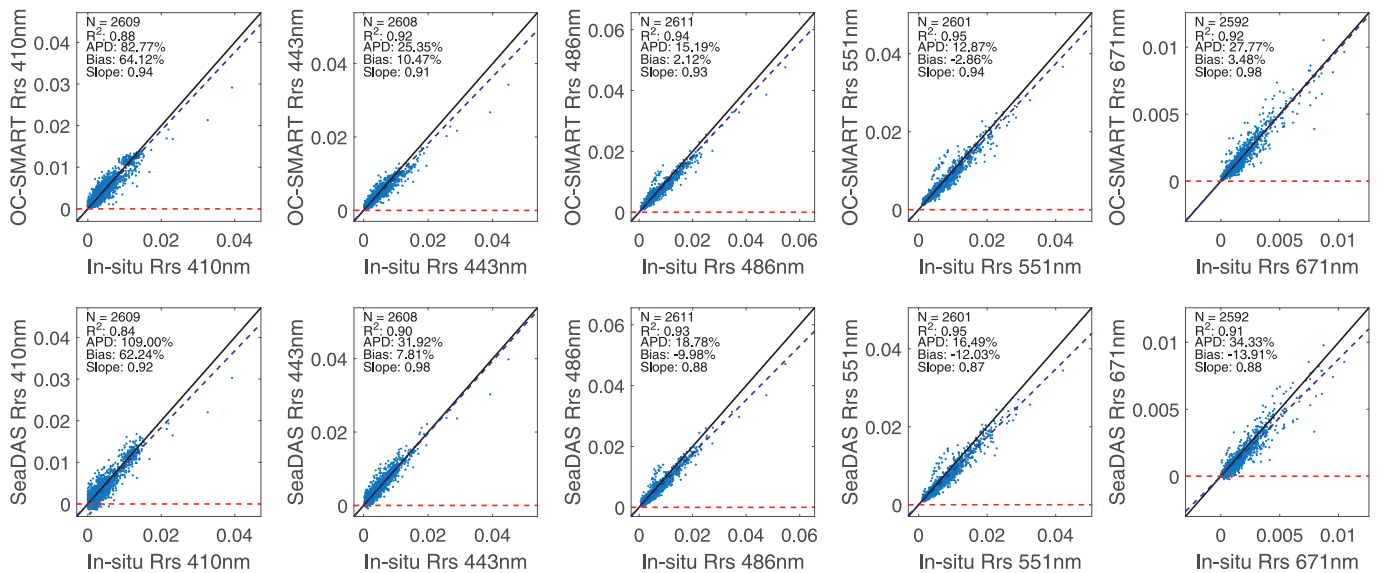
Fig. 7. Validation of R_{rs} retrievals from MODIS images against in-situ measurements. Top: retrieval by OC-SMART, bottom: retrieval by NASA SeaDAS v7.5.2. Data below the red dashed line are negative values. The blue dashed line shows linear regression. (For interpretation of the references to color in this figure legend, the reader is referred to the web version of this article.)

Fig. 8. Validation of R_{rs} retrievals from VIIRS images against in-situ measurements. Top: retrieval by OC-SMART, bottom: retrieval by NASA SeaDAS v7.5.2. Data below the red dashed line are negative values. The blue dashed line shows linear regression. (For interpretation of the references to color in this figure legend, the reader is referred to the web version of this article.)

could be partially due to the relatively low SNR of the sensor, which requires more pixels to be aggregated to meet the required accuracy in the retrievals, as suggested by Bailey and Werdell (2006); Pahlevan et al. (2017b). Therefore, averaging over a box of 5×5 pixels extracted from the satellite retrievals may not be sufficient for those two sensors.

4.2. 4.Validation of OC-SMART ocean IOP retrievals

The ocean IOP retrievals, i.e. a_{ph}, a_{dg}, and b_{bp}, obtained by OC-SMART applied to SeaWiFS data were validated using the validation dataset processed by NASA OBPG, which includes in-situ IOP measurements compiled in the SeaBASS database. The number of in-situ IOP measurements was too low for the other sensors to make a meaningful validation. Fig. 9 shows the location of the in-situ ocean IOP

measurements. The validation results are shown in Fig. 10–12 with details provided in Table S7 (see supplementary material available online). The ocean IOP retrievals obtained using the SeaDAS AC and GIOP algorithms are also provided for comparison. It is quite clear that OC-SMART significantly improved the retrieval of ocean IOPs in all bands compared with the results obtained using the SeaDAS AC and GIOP algorithms. For a_{ph}, OC-SMART increased the R^2 correlation by a factor 1.9–2.7 and reduced the APD by 80% - 260%. For a_{dg}, OC-SMART increased the R^2 correlation by a factor 1.7–2.7 and reduced the APD by 90% - 300%. For b_{bp}, OC-SMART increased the R^2 correlation by up to a factor 4.4 and reduced the APD by about 4% on average. The improvements of the ocean IOP retrievals provided by OC-SMART are due to the following two principal reasons:
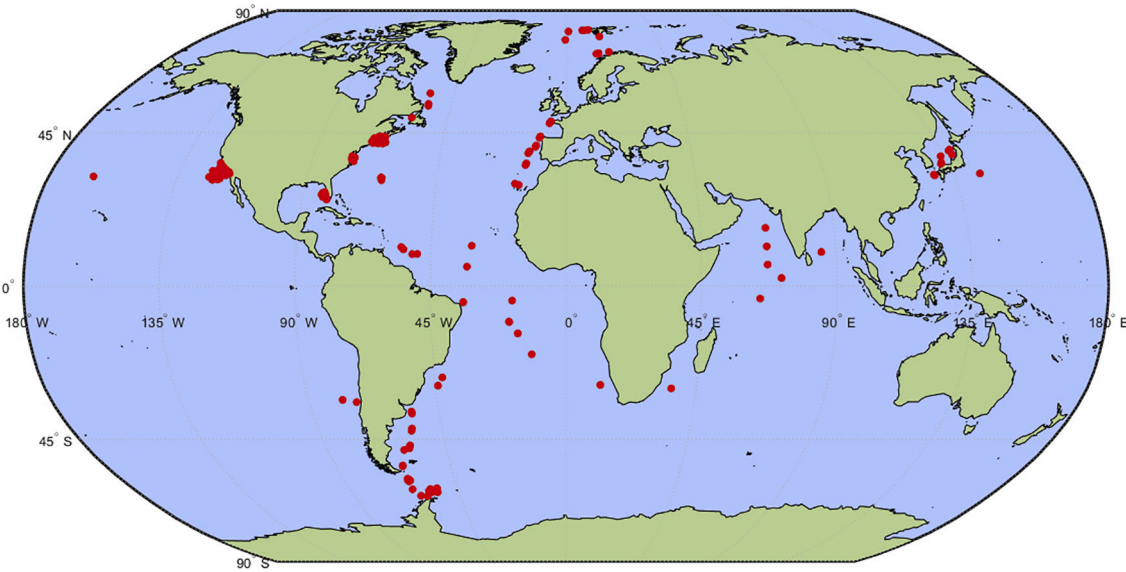
Fig. 9. Location of the in-situ ocean IOP measurements used for validation of satellite OC retrievals produced by OC-SMART and the AC and GIOP algorithms available in SeaDAS v7.5.2.
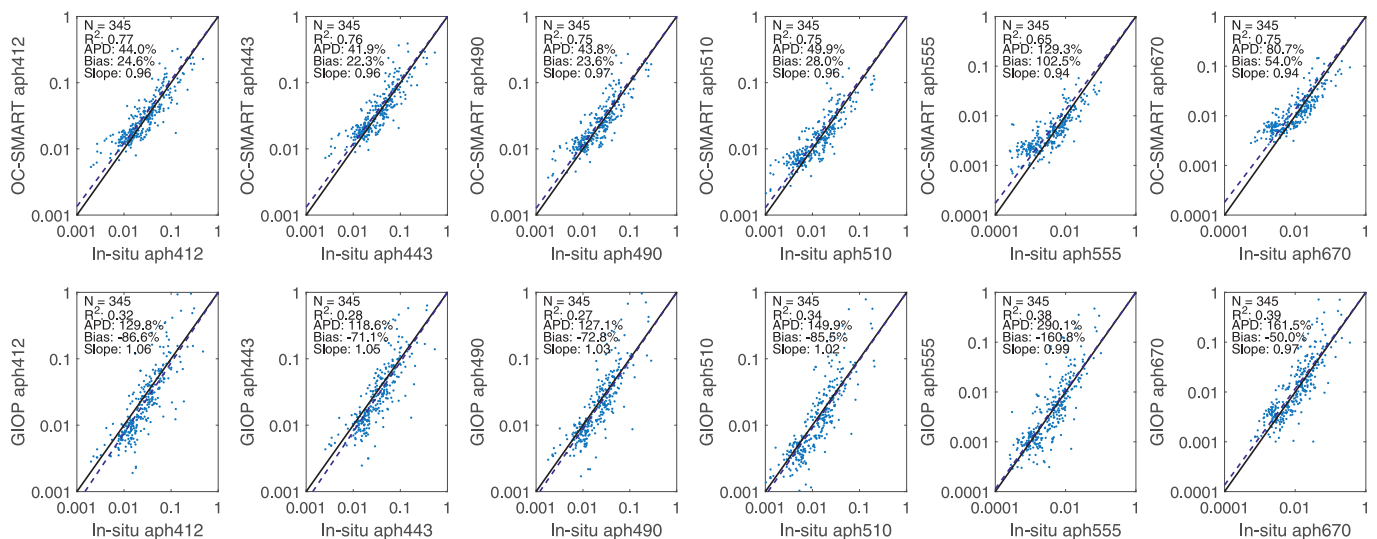

Fig. 10. Validation of the absorption by phytoplankton (a_{ph}) from SeaWiFS images against in-situ measurements. Top: retrieval by OC-SMART, bottom: retrieval by AC and GIOP algorithms available in NASA SeaDAS v7.5.2. The blue dashed line shows linear regression. (For interpretation of the references to color in this figure legend, the reader is referred to the web version of this article.)

1. improved R_{rs} retrievals from our machine learning based global AC algorithm compared to the SeaDAS AC algorithm.
2. a comprehensive ocean IOP dataset used to generate accurate radiative transfer simulations combined with powerful machine learning techniques.

In fact, the negative R_{rs} retrievals produced by the heritage AC algorithm in SeaDAS have significantly reduced the data quality of ocean IOP retrievals derived from the GIOP algorithm. After excluding the cases with negative R_{rs} values, the performance of the GIOP algorithm also increased significantly, as shown in Table S7 (see supplementary material available online). However, the performance of the ocean IOP algorithms still needs to be improved, especially for b_{bp}. Also, a_{dg} decreases exponentially with wavelength and its value becomes relatively small at 670 nm, which makes retrieval difficult.

4.3. Application to geostationary satellite data

The Geostationary Ocean Color Imager (GOCI) is the first dedicated ocean color sensor deployed onboard a geostationary satellite. The GOCI sensor significantly increased the temporal resolution of ocean color products and facilitates studying the short-term variation of the marine ecosystem. However, the field of view of the GOCI sensor covers an area with complex marine conditions including clean oceanic water, turbid continental shelf water, highly dynamic coastal water due to strong tidal currents, extreme turbid estuary areas with total suspended matter (TSM) as high as 5000 [mg/L] (He et al., 2013), and several inland lakes. In the winter to spring season, polluted continental aerosols, fogs, and sandstorms are often observed in the area. The complexity of the atmospheric and marine conditions requires accurate and reliable AC algorithms to ensure good data quality of the ocean color products. The current AC algorithm implemented in the GOCI Data Processing System
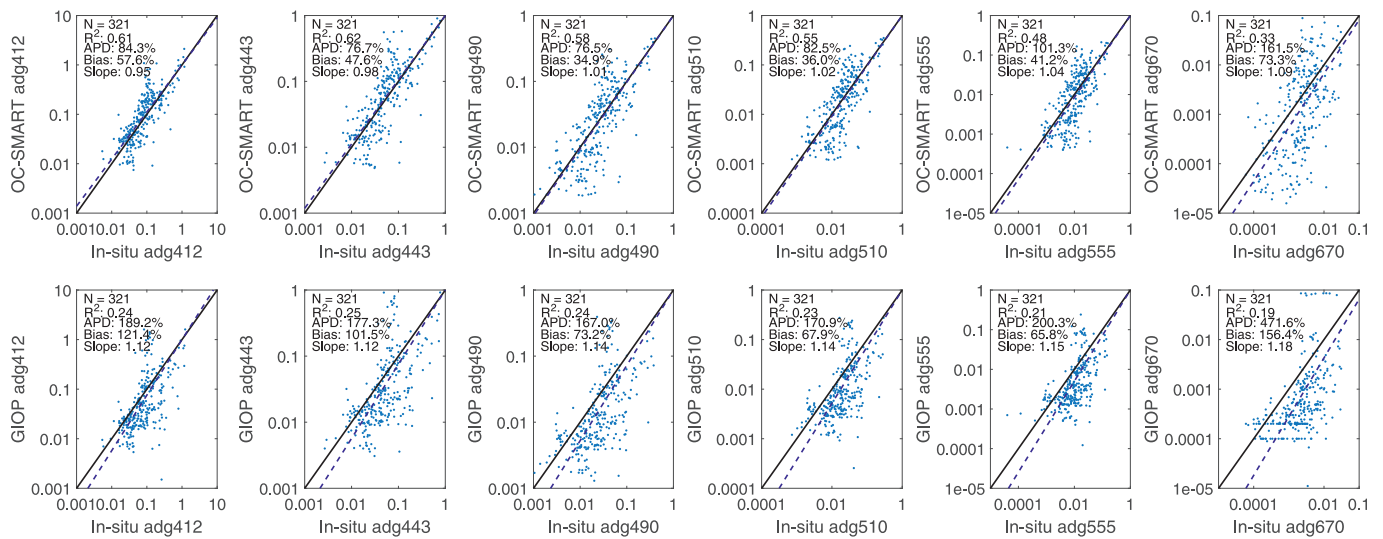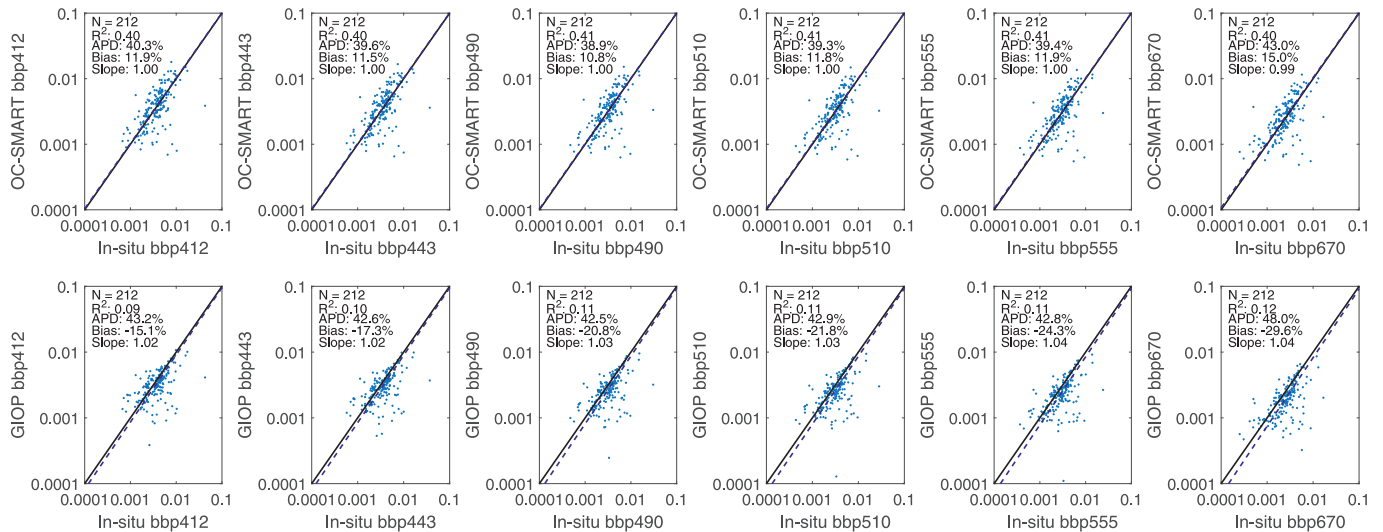
Fig. 11. Validation of the absorption by detritus and Gelbstoff (a_{dg}) from SeaWiFS images against in-situ measurements. Top: retrieval by OC-SMART, bottom: retrieval by AC and GIOP algorithms available in NASA SeaDAS v7.5.2. The blue dashed line shows linear regression. (For interpretation of the references to color in this figure legend, the reader is referred to the web version of this article.)

Fig. 12. Validation of the particulates backscattering (b_{bp}) from SeaWiFS images against in-situ measurements. Top: retrieval by OC-SMART, bottom: retrieval by AC and GIOP algorithms available in NASA SeaDAS v7.5.2. The blue dashed line shows linear regression. (For interpretation of the references to color in this figure legend, the reader is referred to the web version of this article.)

(GDPS) developed by KIOST is a modified version of the heritage algorithm (Ahn et al., 2012), with an improved technique to estimate aerosol information (Ahn et al., 2016). OC-SMART has been modified to support the GOCI mission and the current machine learning based AC algorithm for GOCI will also be implemented in GDPS in the updated version. The machine learning based AC algorithm for GOCI-II will also be implemented in the GOCI-II data processing system.

The Korea Institute of Ocean Science and Technology (KIOST) has conducted a large number of field campaigns in coastal and open ocean waters around Korea and obtained 421 in-situ above-water radiometric measurements since 2010. The remote-sensing reflectance, R_{rs}, was measured by ASD-FieldSpec and TriOS-RAMSES hyperspectral radiometers. Of the 421 samples, 337 spectra were discarded by the strict quality-control process recommended by Moon et al. (2012), which left 84 samples for the match-up process and analysis. Of those 84 samples, most of the shipboard data were collected from highly to moderately turbid waters (Ahn et al., 2015). The location of the in-situ

measurements is shown as red dots in Fig. 13. Three AERONET-OC stations (i.e. Socheongcho, Gageocho, and Ieodo) are located within the field of view of the GOCI sensor. A total of 130 quality-assured level 2.0 measurements were selected from the 3 stations to validate the R_{rs} retrievals. The AERONET-OC measurements were linearly interpolated to the GOCI wavelengths for comparison with satellite retrievals. The location of the AERONET-OC stations is shown as red crosses in Fig. 13. The validation results of the R_{rs} values retrieved by OC-SMART and GDPS v2.0 are shown in Fig. 14 with details provided in Table S8 (see supplementary material available online). Based on the validation results, OC-SMART performs slightly better than GDPS, especially at 412 nm. However, the number of qualified matchup data from GDPS retrievals (i.e. 130 matchups for AERONET-OC) are 35% smaller than for OC-SMART (i.e. 200 matchups for AERONET-OC) due to aggressive cloud masking and atmospheric correction failures. Therefore, use of the MLNN based AC algorithm available in OC-SMART could potentially recover a significant amount of ocean color retrievals from GOCI images.
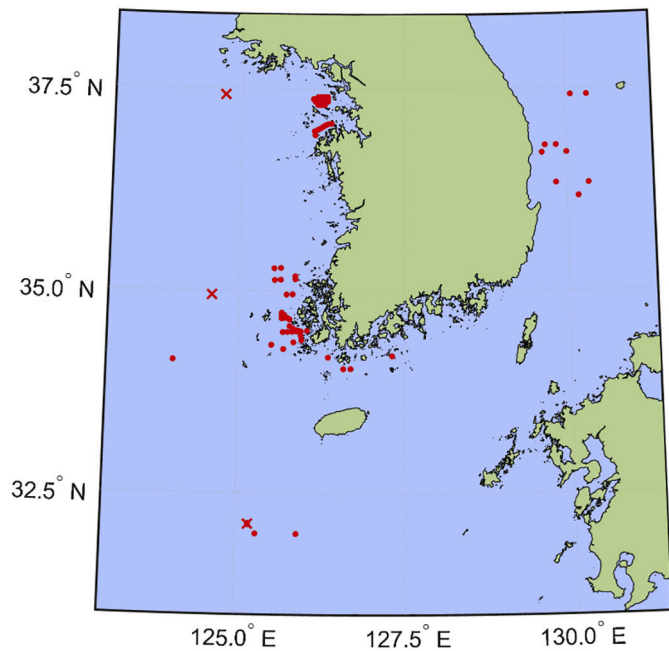
Fig. 13. Location of the field measurements made by KIOST (dots) and AERONET-OC stations (crosses) used for validation of satellite retrievals from the GOCI sensor by OC-SMART and GDPS 2.0.

4.4. Application to hyperspectral sensors

Current ocean color sensors reveal the quantity of phytoplankton in the ocean surface layer, but have yet to determine the diversity of species. The Ocean Color Instrument (OCI) onboard the future Plankton, Aerosol, Cloud, ocean Ecosystem (PACE) mission spacecraft will provide hyper-spectral measurements (i.e. 5 nm spectral resolution from 340 nm to 890 nm) of the global ocean every 1–2 days. Hence, the PACE mission has the potential to improve estimates of the phytoplankton community composition and also improve the discrimination of biogenic constituents in the ocean (e.g., UV measurements will improve the separation of absorption by the colored dissolved organic matter (CDOM) and absorption by phytoplankton).

To explore the feasibility of applying our machine learning algorithms to hyper-spectral measurements, we developed a preliminary machine learning based AC and ocean IOP algorithm for the Hyper-spectral Imager for the Coastal Ocean (HICO), the first spaceborne imaging spectrometer designed to sample the coastal ocean (Corson et al., 2008; Lucke et al., 2011). Deployed onboard the International Space Station (ISS), HICO samples selected coastal regions at 90 m spatial resolution with a very high signal-to-noise ratio (SNR) to resolve the complexity of the coastal ocean. The spectral range of HICO is 350–1080 nm with a sampling interval of 5.7 nm. However, the best data provided by HICO lie in the 400–900 nm spectral range; data obtained outside this spectral range are less accurate (Lucke et al., 2011; Ibrahim et al., 2018). We developed preliminary versions of our machine learning based AC and ocean IOP retrieval algorithms for HICO for the 400–900 nm spectral range. The algorithms will be extended to the UV range in a forthcoming version. Gaussian functions centered at each HICO band with a FWHM of 10 nm for the 400–745 nm spectral range and 20 nm for the 745–900 nm spectral range were used as the relative spectral response functions in the radiative transfer simulations. A few bands that are affected by water vapor (i.e. around 725 nm and 825 nm) and oxygen absorption (i.e. around 765 nm) were also excluded in the preliminary version of the algorithms.

Fig. 15 shows one example of ocean color products retrieved by OC-SMART and NASA SeaDAS from HICO images over Chesapeake Bay on March 13, 2014. The RGB image composed from R_{rs} retrievals, i.e. panels (b) and (g), shows that the heritage algorithm in SeaDAS does not work in highly turbid waters and yields some areas with no retrievals (red circled areas) in all the ocean color products. A closer inspection of the area indicated that these pixels failed the atmospheric correction algorithm, marked by the flag ATMFAIL in SeaDAS. In contrast, OC-SMART works well in both highly turbid and moderately turbid coastal waters. Comparison of the ocean IOP products, i.e. panel (c) - (e) and (h) - (i), show that in addition to the "no retrieval" issue in highly turbid water, the GIOP algorithm in SeaDAS failed in some coastal areas (marked by green circles). A closer inspection showed that negative nR_{rs} values were retrieved by the SeaDAS AC algorithm in the UV and blue bands which may explain the failure of the GIOP algorithm. Another issue with the GIOP algorithm in this particular case is that the eigenvectors of the 3 ocean IOPs may not be suitable, especially in the open water area outside Chesapeake Bay, which may lead to an overestimation of retrieved a_{ph} values and an underestimation of retrieved
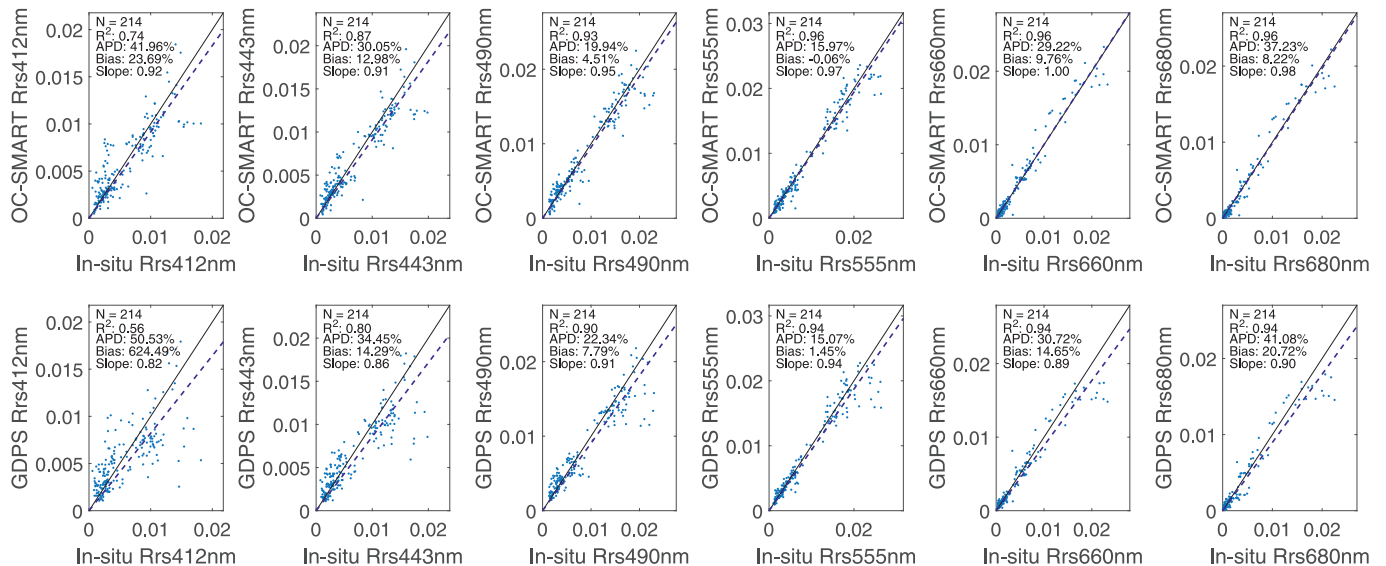

Fig. 14. Validation of R_{rs} retrievals from GOCI images against in-situ measurements. Top: retrieval by OC-SMART, bottom: retrieval by GDPS v2.0. The blue dashed line shows linear regression. (For interpretation of the references to color in this figure legend, the reader is referred to the web version of this article.)
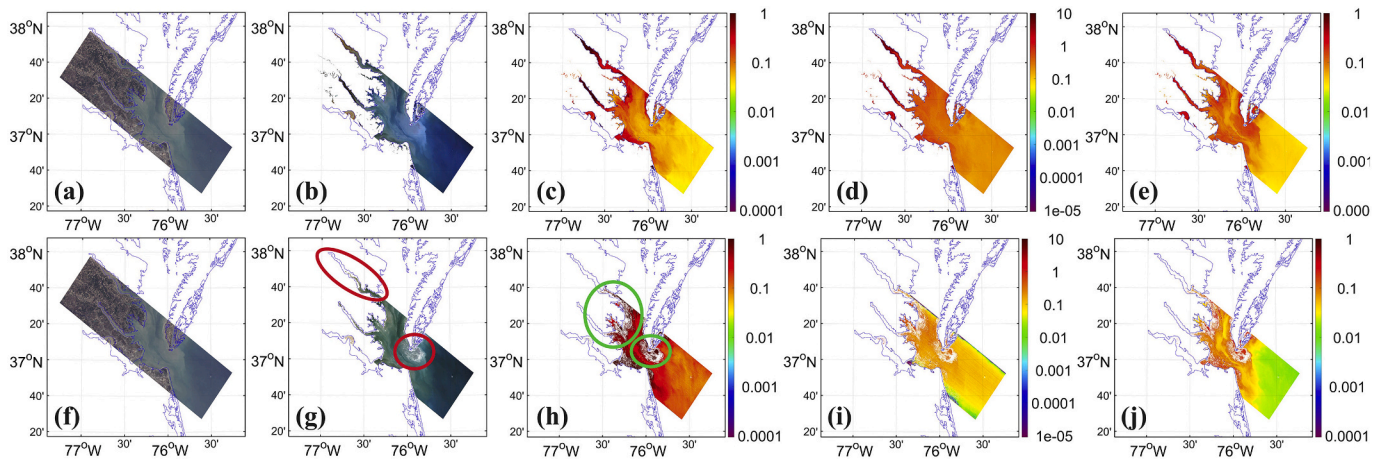
Fig. 15. Comparison of ocean color products retrieved by OC-SMART (top panels) and NASA SeaDAS (bottom panels) from HICO images on March 13, 2014. (a) and (f): RGB composed from TOA reflectance at 473 nm, 553 nm and 650 nm; (b) and (g): RGB composed from R_{rs} retrievals at 473 nm, 553 nm and 650 nm; (c) and (h): retrieved a_{ph} at 444 nm; (d) and (i): retrieved a_{dg} at 444 nm; (e) and (j): retrieved b_{bp} at 444 nm.

a_{dg} values. For example, panels (h) and (i) show a much lower value in the a_{dg} retrieval and much higher value in the a_{ph} retrieval from the GIOP algorithm. In contrast, the ocean IOPs retrieved by OC-SMART appear to be quite reasonable for this case.

5. Discussion

The machine learning technology has been successfully applied to many aspects of our modern life. In this paper, we have created a framework for application of machine learning algorithms to global ocean color missions and demonstrated their superiority over heritage algorithms. In particular, a well trained machine learning algorithm is more resilient to noise in satellite measurements (see Section 5.1), and the non-uniqueness of the retrievals appears not to be a serious issue, as discussed in Section 5.2.

5.1. Sensor signal to noise ratio (SNR) requirements

Satellite measurements always have inherent noise including shot noise, readout noise, dark noise, etc. Most heritage algorithms do not have the capability to handle noise in satellite measurements, and

therefore require the sensor to have a very high SNR, i.e. larger than 400 (Qi et al., 2017). If properly trained, a machine learning algorithm is capable of extracting information from noisy data accurately, due to its interpolation capability, and is applicable to sensors with SNR as low as 50. Therefore, another important improvement that we made to the training process is to incorporate the sensor SNR in the training data. The SNR of a satellite sensor is usually given at a typical radiance level ($L_{typical}$). However, the actual SNR is not a constant, implying that if the satellite-measured radiance is lower than $L_{typical}$, then the SNR is also lower. Therefore, when adding noise to the training dataset, an appropriate noise level must be established. The published SNR values at $L_{typical}$ should not be used, because the MLNN will not be able to learn to handle the larger noise associated with pixels that have radiances lower than $L_{typical}$. In principle, the lowest possible SNR should be used, however, if the SNR is too low, the training accuracy also decreases, implying that the trained MLNN will have a low sensitivity that will affect the quality of the retrieved ocean color products. To find a good balance between noise handling capability and feature sensitivity, we tested the performance of the MLNN with different SNR settings and found that a SNR level between 50 and 100 (i.e. adding 1–2% of noise to the TOA radiances) is adequate for many ocean color sensors. Therefore,
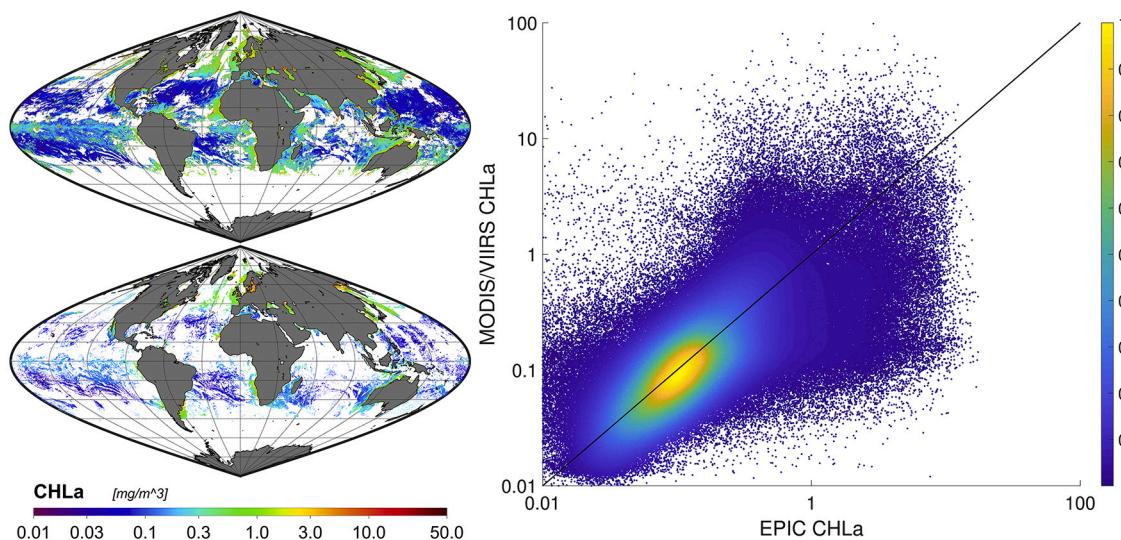

Fig. 16. Top left: daily global CHL product on May 23, 2018 retrieved from EPIC by OC-SMART. Bottom left: daily global CHL product on May 23, 2018 retrieved from MODIS and VIIRS by SeaDAS. Right: scatterplot of the CHL product retrieved from EPIC and combined MODIS/VIIRS. The color of the plot means data density.

Gaussian distributed noise with a standard deviation matching the selected SNR, is added independently to the TOA radiances at all wavelengths before the training.

The ability to handle noise in the input data is one of the biggest advantages of machine learning algorithms. To demonstrate this advantage, we applied our machine learning algorithms to the Earth Polychromatic Imaging Camera (EPIC) onboard the Deep Space Climate Observatory (DSCOVR) (Marshak et al., 2018). The EPIC sensor does not have the proper NIR or SWIR bands required by the heritage algorithms for aerosol model estimation and the SNR of the EPIC sensor may be as low as 50 (personal communication with members of the EPIC Science team). Therefore, the heritage algorithms are not suitable for analysis of EPIC data. Gao et al. (2019) recently attempted retrieval of ocean color products from EPIC using a heritage algorithm, and showed that the heritage algorithm is unable to retrieve real time aerosol information from EPIC images. Therefore, climatology aerosol models and aerosol optical depths were used in the study reported by Gao et al. (2019).

Our machine learning based AC algorithm does not depend on NIR or SWIR spectral bands, and is therefore applicable to EPIC. We used a SNR level of 50 when training the AC algorithm for EPIC. The retrieved daily global CHL product on May 23, 2018 is shown in top left panel of Fig. 16. For comparison, the daily global chlorophyll_a concentration (CHL) product from combined MODIS and VIIRS retrievals using heritage algorithms is also shown in the bottom left panel of Fig. 16. A scatterplot of the two CHL products is shown in the right panel of Fig. 16. The color of the plot means data density. There is a very good agreement between the two daily global CHL products and the significantly increased spatial coverage in the EPIC CHL product is due to the high temporal resolution of the EPIC sensor. This result demonstrates that a machine learning algorithm is capable of retrieving high quality ocean color products from low SNR sensors that are normally considered difficult (if not impossible) to retrieve by heritage algorithms.

5.2. Uniqueness of retrieval from machine learning algorithms

Inverse methods are aimed at retrieving a set of state parameters (e. g. aerosol optical depths, remote sensing reflectances, etc.) from satellite measured top-of-atmosphere (TOA) reflectances. However, a different set of state parameters could (within the noise level) be associated with similar spectral TOA reflectances. This non-uniqueness of the retrieved state parameters becomes a problem if the inverse method was unable to retrieve the correct set of parameters. To evaluate the performance of the machine learning algorithm under such conditions, we searched through our training dataset to identify any two cases that have similar spectral Rayleigh corrected TOA reflectances (L_{rc} values). Then, we applied OC-SMART to retrieve the spectral AOD and R_{rs} values from the identified cases and compared the retrieval with the true values (i.e. the input values used in the RT simulations). Fig. 17 shows some examples of the identified non-unique cases and the comparison between OC-SMART retrievals and the true values. The upper panels show the comparison of the two spectral L_{rc} values. The band-averaged percentage difference between the two cases is less than 0.5% for open ocean cases (first 3 panels), and less than 1.3% for coastal water cases (last 3 panels). The middle panels show a comparison between the retrieved AOD values (dashed lines) and the true values (solid lines). The lower panels show the same as the middle panels but for R_{rs} values. The comparison shows that the machine learning algorithm was able to retrieve the correct set of AOD and R_{rs} values from similar spectral L_{rc}. The reason is that even though the spectral L_{rc} values are similar between the two cases, other parameters, such as geometry angles and relative humidity (RH), are different. Therefore, the correct set of AOD and R_{rs} values associated with each case can be retrieved by the machine learning algorithm in OC-SMART, since it takes geometry angles and RH into account. Therefore, in addition to the spectral remote sensing reflectances, other parameters are required to help resolve the non-uniqueness issue in the inverse problem. We have also discovered that the chance of identifying two cases with similar spectral L_{rc} values is very low, about 1 in 1 million paired cases. Therefore, the training dataset for the machine learning algorithm must be large enough so that the non-unique cases have sufficient appearance for the machine learning algorithm to learn its pattern. We believe that there could be cases when the machine learning algorithm was unable to retrieve the
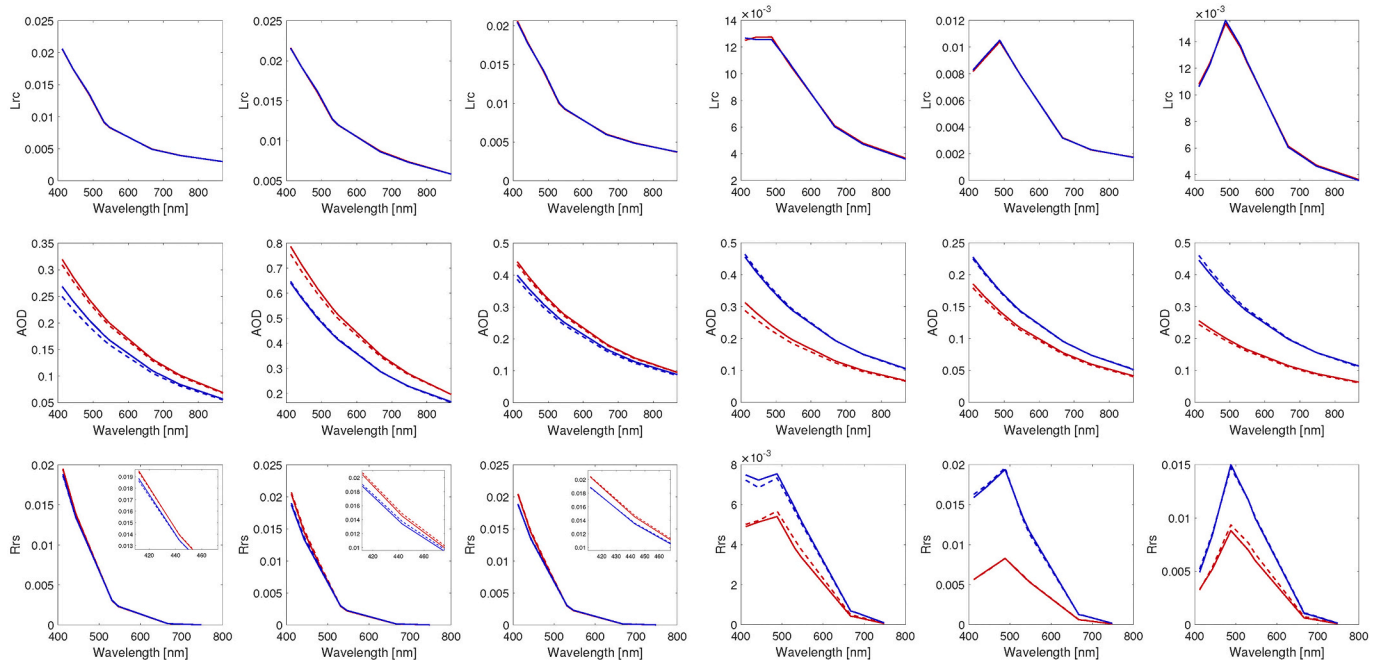

Fig. 17. Case study of the non-uniqueness issue of the machine learning algorithm for open ocean (first 3 columns) and coastal water (last 3 columns) cases. Upper panels: Comparison of the two cases with similar Rayleigh corrected TOA radiances (L_{rc}). Middle panels: Comparison of the AOD values retrieved by the AOD MLNN of the two cases. Solid lines are the true values (i.e. input values used in the RT simulations) and the dashed lines are the retrievals by the AOD MLNN. Lower panels: Similar as the middle panels but for R_{rs} retrievals; the inset at the upper right corner of the first 3 panels is an enlargement to show the details.

correct set of state parameters. However, it does not seem to be a severe problem for OC-SMART, and with larger and more comprehensive training datasets and additional input parameters, such as polarization, the impact of the non-uniqueness issue may be minimized.

6. Future directions

6.1. Vector radiative transfer simulations

In this paper we have used a scalar radiative transfer (RT) code for a coupled atmosphere-ocean system to create simulated datasets used for training of machine learning algorithms, except for the Rayleigh scattering corrections that rely on polarized (vector) RT simulations. We have developed a fully polarized RT model that is implemented in AccuRT (Stamnes et al., 2018a). However, it is still premature to utilize a polarized RT model to generate comprehensive RT simulation dataset required by the neural network training. One particular issue is the lack of good quality measurement data to construct realistic phase matrices for both open ocean and coastal waters. Once such data becomes available, we will use the polarized RT model for the RT simulations. We expect that use of fully polarized RT simulations will lead to further improvements in retrieval results as discussed elsewhere (Stamnes et al., 2018b, 2018c).

6.2. Correction for earth curvature effects

Satellite images acquired in the polar regions or near sunrise and sunset (i.e. for geostationary satellites) often have solar zenith angles larger than 75°. Ocean color products retrieved by current AC algorithms typically have large uncertainties under such conditions, due to inadequacies related to both forward and inverse modeling. In the forward RT model, the *plane-parallel approximation* (PPA) becomes invalid for solar zenith angles larger than about 75° (and large viewing angles). Therefore, we need to take Earth curvature into account as discussed by He et al. (2018). An approximate way to deal with this problem is the so-called *pseudo-spherical approximation* (PSA), in which the last term of Eq. (2). i.e. the direct beam single-scattering (solar pseudo-source) term is treated in spherical geometry by letting $e^{-\tau/\mu_0} \rightarrow e^{-\tau Ch(\mu_0)}$ in Eq. (2). In
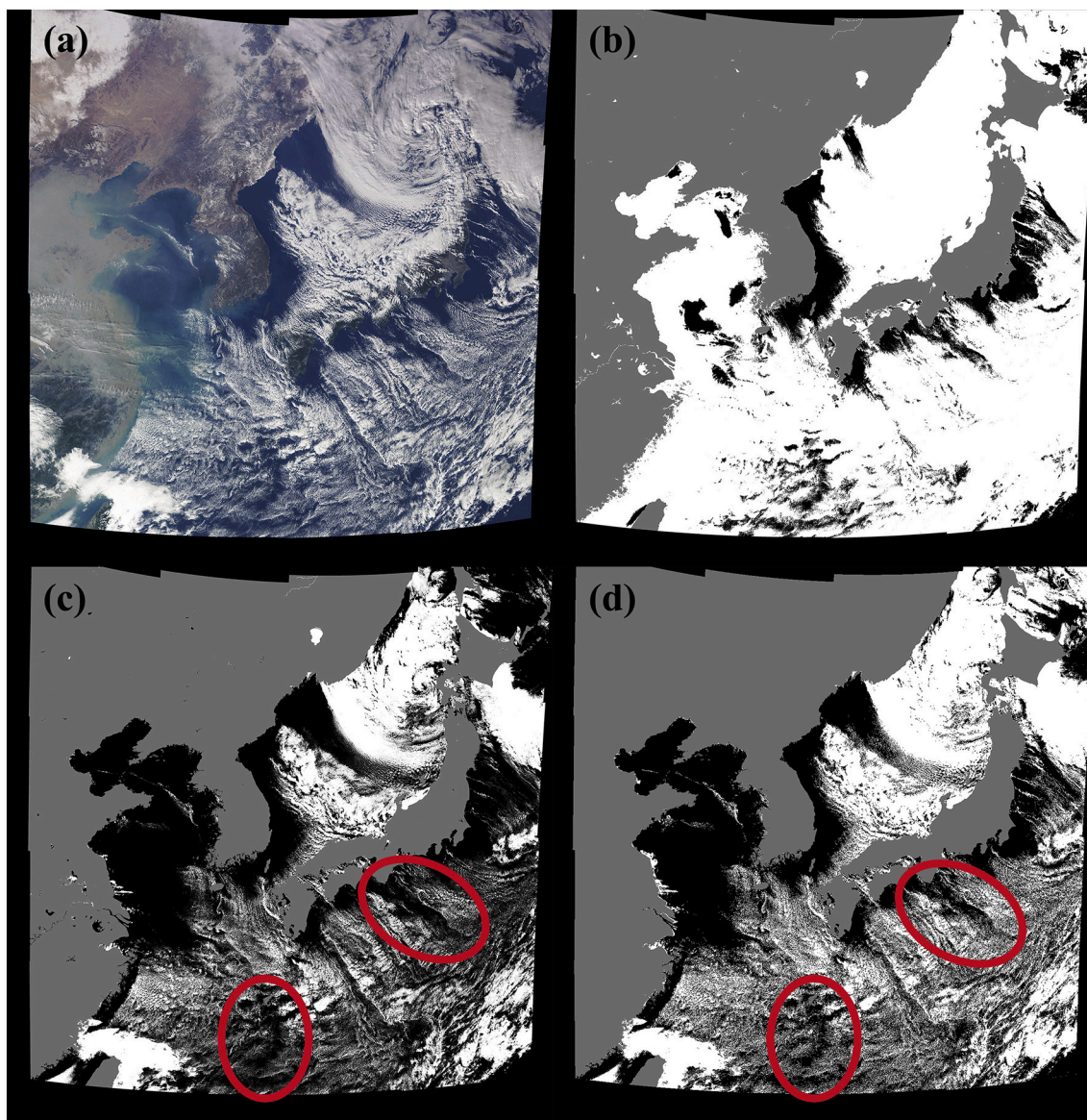

Fig. 18. Comparison of cloud mask algorithms applied to a GOCI image on 01/01/2018 at 05:16 UTC. (a) is a GOCI RGB image; (b), (c), and (d) are cloud mask results obtained from STDCM, N09CM, and MLCM, respectively. Red circled areas in panels (c) and (d) show better cloud edge detection of the MLCM compared to N09CM. (For interpretation of the references to color in this figure legend, the reader is referred to the web version of this article.)

the PSA the Chapman function $Ch(\mu_0)$ takes curvature into account (Stamnes et al., 2017; He et al., 2018), while the multiple scattering term is treated using the PPA. For the inverse modeling, one challenge is that removal of the Rayleigh reflectance from the total TOA reflectance becomes more difficult and may yield negative values (He et al., 2018). Therefore, for large solar zenith angles the total TOA reflectance must be used to train the neural network. Hence, to account for Earth curvature effects, we will invoke the pseudo-spherical approximation in the forward RT simulation and develop a new algorithm to derive remote sensing reflectances from total TOA reflectances, without removing the Rayleigh contribution.

6.3. Cloud mask improvements

Most current cloud screening methods employ thresholds based on empirical or statistical analyses of data from a specific area, implying that it may be questionable to apply such a threshold to a different area and under different solar/viewing geometries. Exploiting advances in machine learning techniques, we have developed a new, threshold-free cloud mask algorithm (MLCM) based on a neural network classifier driven by extensive RTM simulations (Chen et al., 2018). We generated a large dataset which covers as many combinations of water/aerosol/cloud configurations as deemed desirable and used advanced machine learning algorithms to classify these cases. Compared to traditional methods, MLCM has no fixed thresholds, and can be applied to any area of the world for any sun-sensor geometry.

Fig. 18 shows a comparison of STDCM, N09CM, and MLCM cloud mask results for a GOCI image obtained on 01/01/2018 at 05:16 UTC. Panel (a) is the GOCI RGB image, panels (b), (c), and (d) are the cloud mask results obtained by STDCM, N09CM, and MLCM, respectively. It is clear that the STDCM misidentified most of the pixels in the coastal area. The N09CM and MLCM cloud masks yielded very similar results and both correctly identified the cloudy pixels in the coastal area. However, the MLCM performs significantly better than N09CM at large solar and viewing zenith angles (i.e. $\theta_0 > 70°$ and $\theta > 50°$, see upper right corner of panel (c) and (d) in Fig. 18). The large errors in ρ_{rc} (due to lack of consideration of the Earth curvature effect at large SZAs) used in N09CM may have been the reason for this type of mis-classification. The MLCM is trained by TOA radiances instead of ρ_{rc} to avoid possible errors introduced by the use of Rayleigh-corrected radiances at large SZAs (He et al., 2018). In addition, tests have shown that MLCM better identifies cloud edges compared to N09CM which can be seen in the bottom and right part of Fig. 18, circled in red. We note that MLCM has some misclassification over the coastal area of East China with either extremely turbid or shallow water. This misclassification suggests that we need to improve the MLCM by including RT simulations of such extreme cases in the training dataset. The MLCM is currently under final assessment and will be implemented in OC-SMART to replace N09CM in future versions.

6.4. Bayesian uncertainty estimation

It is desirable to provide uncertainties on a per-pixel basis for satellite retrievals, however, it is a difficult task for a neural network designed as a regressor, which typically returns a single predicted value rather than a probability distribution. To obtain uncertainty estimates on a per-pixel basis we adopted a Bayesian approach in which uncertainties in measured TOA radiances and a priori information are used to quantify uncertainties in the retrieval parameters delivered by OC-SMART. The Bayesian uncertainty estimation algorithm is currently under final assessment and will be implemented in OC-SMART in future versions.

7. Summary and conclusions

In this paper, we described the methodology and implementation of machine learning based AC and ocean IOP algorithms for global ocean

color applications. The algorithms are developed based on extensive radiative transfer simulations of a coupled atmosphere-ocean system. Multiple atmosphere, aerosol and ocean IOP models were adopted to create a large, comprehensive, and realistic dataset used for training. The algorithms have been implemented in a new multi-sensor platform, OC-SMART, for ocean color data retrievals from images obtained by satellite remote sensing instruments. Compelling features of OC-SMART can be summarized as follows:

- Global application: OC-SMART is applicable in both open ocean and coastal/inland waters, as well as in extreme conditions such as heavy aerosol loadings, extremely turbid water, etc.
- Reliability: OC-SMART provides a complete resolution of the negative water-leaving signal issue which plagues heritage AC algorithms.
- Flexibility: The framework of OC-SMART is, in principle, applicable to any suitable combination of spectral bands but requires some effort in forward/inverse modeling and validation to fully integrate a new sensor.
- Noise handling: OC-SMART appears to be weakly affected by noise in the satellite measurements and therefore applicable to sensors with low signal to noise ratio (SNR).
- Accuracy: OC-SMART provides improved retrievals of water-leaving radiances and ocean IOPs compared to the heritage algorithms, especially in complex coastal and inland water areas.
- Robustness: OC-SMART appears to be robust and resilient to contamination due to sunglint and adjacency effects of land or cloud edges based on extensive testing (not documented in this paper).
- Efficiency: OC-SMART is fast (about 10 times faster than NASA's SeaDAS package) and suitable for operational use.
- Multi-sensor support: OC-SMART currently supports 11 sensors: SeaWiFS, Aqua/MODIS, SNPP/VIIRS, ISS/HICO, Landsat8/OLI, DSCOVR/EPIC, Sentinel-2/MSI, Sentinel-3/OLCI, COMS/GOCI, GCOM-C/SGLI and FengYun-3D/MERSI2.

OC-SMART is currently available as a standalone Python package or as a plugin that can be installed in ESA's SNAP platform (http://www.rtatmocn.com/oc-smart/).

The remote sensing reflectance (R_{rs}) and ocean IOP products (i.e. a_{ph}, a_{dg} and b_{bp}) retrieved by OC-SMART from images taken by SeaWiFS, MODIS, and VIIRS are validated using a global dataset that include in-situ measurements from MOBY, SeaBASS, and AERONET-OC stations. The ocean color products retrieved by the heritage algorithms implemented in NASA's SeaDAS package are also provided for comparison. The results show that OC-SMART improved R_{rs} retrievals for all the three sensors, especially in blue and red bands where OC-SMART reduces APD by up to 25%. Comparison of the ocean IOP products shows a significant improvement obtained by OC-SMART compared with the SeaDAS AC + GIOP algorithms. A closer inspection shows that the negative R_{rs} issue has greatly degraded the performance of the GIOP algorithm.

In Section 5.1, we discussed the signal to noise ratio (SNR) requirement for machine learning (ML) based algorithms and showed that ML algorithms can deal with or tolerate much lower SNR levels than heritage algorithms which have limited ability to handle noise in the satellite measurements. Non-uniqueness of the retrievals obtained by ML algorithms appears not to be a serious issue, as discussed in Section 5.2.

In Section 6 we discussed some important remaining topics to be addressed in future developments of OC-SMART, such as use of vector rather than scalar RT forward model simulations, application to large solar zenith angle conditions, cloud screening over turbid coastal/inland waters, and application of the Bayesian approach to uncertainty estimation. These topics constitute possible directions for future developments of OC-SMART and similar ocean color algorithms.

Declaration of Competing Interest

The authors declare that they have no known competing financial interests or personal relationships that could have appeared to influence the work reported in this paper.

Acknowledgements

Appendix A. Supplementary data

Supplementary data to this article can be found online at https://doi.org/10.1016/j.rse.2020.112236.

References

Abadi, M., Agarwal, A., Barham, P., Brevdo, E., Chen, Z., Citro, C., Corrado, G.S., Davis, A., Dean, J., Devin, M., Ghemawat, S., Goodfellow, I., Harp, A., Irving, G., Isard, M., Jia, Y., Jozefowicz, R., Kaiser, L., Kudlur, M., Levenberg, J., Mané, D., Monga, R., Moore, S., Murray, D., Olah, C., Schuster, M., Shlens, J., Steiner, B., Sutskever, I., Talwar, K., Tucker, P., Vanhoucke, V., Vasudevan, V., Viégas, F., Vinyals, O., Warden, P., Wattenberg, M., Wicke, M., Yu, Y., Zheng, X., 2015. TensorFlow: Large-Scale Machine Learning on Heterogeneous Systems. URL: https://www.tensorflow.org/ software available from tensorflow.org.

Ahmad, Z., McClain, C.R., Herman, J.R., Franz, B.A., Kwiatkowska, E.J., Robinson, W.D., Bucsela, E.J., Tzortziou, M., 2007. Atmospheric correction for no2 absorption in retrieving water-leaving reflectances from the seawifs and modis measurements. Appl. Opt. 46, 6504–6512. URL: http://ao.osa.org/abstract.cfm?URI=ao-46-26-6504. https://doi.org/10.1364/AO.46.006504.

Ahmad, Z., Franz, B.A., McClain, C.R., Kwiatkowska, E.J., Werdell, J., Shettle, E.P., Holben, B.N., 2010. New aerosol models for the retrieval of aerosol optical thickness and normalized water-leaving radiances from the seawifs and modis sensors over coastal regions and open oceans. Appl. Opt. 49, 5545–5560. URL: http://ao.osa.org/abstract.cfm?URI=ao-49-29-5545. https://doi.org/10.1364/AO.49.005545.

Ahn, J.-H., Park, Y.-J., Ryu, J.-H., Lee, B., Oh, I.S., 2012. Development of atmospheric correction algorithm for geostationary ocean color imager (goci). Ocean Sci. J. 47, 247–259. https://doi.org/10.1007/s12601-012-0026-2.

Ahn, J.-H., Park, Y.-J., Kim, W., Lee, B., Oh, I.S., 2015. Vicarious calibration of the geostationary ocean color imager. Opt. Express 23, 23236–23258. URL: http://www.opticsexpress.org/abstract.cfm?URI=oe-23-18-23236. https://doi.org/10.1364/OE.23.023236.

Ahn, J.-H., Park, Y.-J., Kim, W., Lee, B., 2016. Simple aerosol correction technique based on the spectral relationships of the aerosol multiple-scattering reflectances for atmospheric correction over the oceans. Opt. Express 24, 29659–29669. URL: http://www.opticsexpress.org/abstract.cfm?URI=oe-24-26-29659. https://doi.org/10.1364/OE.24.029659.

Amari, S., Park, H., Fukumizu, K., 2000. Adaptive method of realizing natural gradient learning for multilayer perceptrons. Neural Comput. 12, 1399–1409. https://doi.org/10.1162/089976600300015420.

Babin, M., Stramski, D., Ferrari, G.M., Claustre, H., Bricaud, A., Obolensky, G., Hoepffner, N., 2003. Variations in the light absorption coefficients of phytoplankton, nonalgal particles, and dissolved organic matter in coastal waters around europe. J. Geophys. Res. Oceans 108. https://doi.org/10.1029/2001JC000882. 3211 n/a–n/a.

Bailey, S.W., Werdell, P.J., 2006. A multi-sensor approach for the on-orbit validation of ocean color satellite data products. Remote Sens. Environ. 102, 12–23. URL: http://www.sciencedirect.com/science/article/pii/S0034425706000472. https://doi.org/10.1016/j.rse.2006.01.015.

Bailey, S.W., Hooker, S.B., Antoine, D., Franz, B.A., Werdell, P.J., 2008. Sources and assumptions for the vicarious calibration of ocean color satellite observations. Appl. Opt. 47, 2035–2045. URL: http://ao.osa.org/abstract.cfm?URI=ao-47-12-2035. https://doi.org/10.1364/AO.47.002035.

Banks, A.C., Mélin, F., 2015. An assessment of cloud masking schemes for satellite ocean colour data of marine optical extremes. Int. J. Remote Sens. 36, 797–821. https://doi.org/10.1080/01431161.2014.1001085.

Bodhaine, B.A., Wood, N.B., Dutton, E.G., Slusser, J.R., 1999. On rayleigh optical depth calculations. J. Atmos. Ocean. Technol. 16, 1854–1861. https://doi.org/10.1175/1520-0426(1999)016<1854:ORODC>2.0.CO;2.

Chen, J., Quan, W., Cui, T., Song, Q., Lin, C., 2014. Remote sensing of absorption and scattering coefficient using neural network model: development, validation, and application. Remote Sens. Environ. 149, 213–226. URL: http://www.sciencedirect.com/science/article/pii/S0034425714001515. https://doi.org/10.1016/j.rse.2014.04.013.

Chen, N., Li, W., Gatebe, C., Tanikawa, T., Hori, M., Shimada, R., Aoki, T., Stamnes, K., 2018. New neural network cloud mask algorithm based on radiative transfer simulations. Remote Sens. Environ. 219, 62–71.

Clark, D.K., Yarbrough, M.A., Feinholz, M., Flora, S., Broenkow, W., Kim, Y.S., Johnson, B.C., Brown, S.W., Yuen, M., Mueller, J.L., 2003. Moby, a radiometric buoy for performance monitoring and vicarious calibration of satellite ocean color sensors: Measurement and data analysis protocols. In: Ocean Optics Protocols For Satellite Ocean Color Sensor Validation Chapter 2. NASA Technical Reports.

Corson, M.R., Korwan, D.R., Lucke, R.L., Snyder, W.A., Davis, C.O., 2008. The hyperspectral imager for the coastal ocean (hico) on the international space station. In: IGARSS 2008–2008 IEEE International Geoscience and Remote Sensing Symposium (pp. IV – 101–IV – 104), vol. 4. https://doi.org/10.1109/IGARSS.2008.4779666.

Cybenko, G., 1989. Approximation by superpositions of a sigmoidal function. Math. Control Signals Syst. 2, 303–314. URL: https://doi.org/10.1007/BF02551274. https://doi.org/10.1007/BF02551274.

Fan, Y., Li, W., Voss, K.J., Gatebe, C.K., Stamnes, K., 2016. Neural network method to correct bidirectional effects in water-leaving radiance. Appl. Opt. 55, 10–21. URL: http://ao.osa.org/abstract.cfm?URI=ao-55-1-10. https://doi.org/10.1364/AO.55.000010.

Fan, Y., Li, W., Gatebe, C.K., Jamet, C., Zibordi, G., Schroeder, T., Stamnes, K., 2017. Atmospheric correction over coastal waters using multilayer neural networks. Remote Sens. Environ. 199, 218–240. URL: http://www.sciencedirect.com/science/article/pii/S0034425717303310. https://doi.org/10.1016/j.rse.2017.07.016.

Franz, B.A., Bailey, S.W., Werdell, P.J., McClain, C.R., 2007. Sensor-independent approach to the vicarious calibration of satellite ocean color radiometry. Appl. Opt. 46, 5068–5082. URL: http://ao.osa.org/abstract.cfm?URI=ao-46-22-5068. https://doi.org/10.1364/AO.46.005068.

Frouin, R., Schwindling, M., Deschamps, P.-Y., 1996. Spectral reflectance of sea foam in the visible and near-infrared: In situ measurements and remote sensing implications. J. Geophys. Res. Oceans 101, 14361–14371. URL: https://doi.org/10.1029/96JC00629. https://doi.org/10.1029/96JC00629.

Gao, B.-C., Li, R.-R., Yang, Y., 2019. Remote sensing of daytime water leaving reflectances of oceans and large inland lakes from epic onboard the dscovr spacecraft at Lagrange-1 point. Sensors 19. https://doi.org/10.3390/s19051243. URL: https://www.mdpi.com/1424-8220/19/5/1243.

Garver, S.A., Siegel, D.A., 1997. Inherent optical property inversion of ocean color spectra and its biogeochemical interpretation: 1. Time series from the sargasso sea. J. Geophys. Res. Oceans 102, 18607–18625.

Gleason, A.C., Voss, K.J., Gordon, H.R., Twardowski, M., Sullivan, J., Trees, C., Weidemann, A., Berthon, J.-F., Clark, D., Lee, Z.-P., 2012. Detailed validation of the bidirectional effect in various case i and case ii waters. Opt. Express 20, 7630–7645. URL: http://www.opticsexpress.org/abstract.cfm?URI=oe-20-7-7630. https://doi.org/10.1364/OE.20.007630.

Gordon, H.R., 1997. Atmospheric correction of ocean color imagery in the earth observing system era. J. Geophys. Res.-Atmos. 102, 17081–17106. URL: https://doi.org/10.1029/96JD02443. https://doi.org/10.1029/96JD02443.

Gordon, H.R., Wang, M., 1992. Surface-roughness considerations for atmospheric correction of ocean color sensors. 1: The rayleigh-scattering component. Appl. Opt. 31, 4247–4260. URL: http://ao.osa.org/abstract.cfm?URI=ao-31-21-4247. https://doi.org/10.1364/AO.31.004247.

Gordon, H.R., Wang, M., 1994a. Influence of oceanic whitecaps on atmospheric correction of ocean-color sensors. Appl. Opt. 33, 7754–7763. URL: http://ao.osa.org/abstract.cfm?URI=ao-33-33-7754. https://doi.org/10.1364/AO.33.007754.

Gordon, H.R., Wang, M., 1994b. Retrieval of water-leaving radiance and aerosol optical thickness over the oceans with seawifs: a preliminary algorithm. Appl. Opt. 33, 443–452. URL: http://ao.osa.org/abstract.cfm?URI=ao-33-3-443. https://doi.org/10.1364/AO.33.000443.

He, X., Bai, Y., Pan, D., Huang, N., Dong, X., Chen, J., Chen, C.-T. A., Cui, Q., 2013. Using geostationary satellite ocean color data to map the diurnal dynamics of suspended particulate matter in coastal waters. Remote Sens. Environ. 133, 225–239. URL: http://www.sciencedirect.com/science/article/pii/S0034425713000503. https://doi.org/10.1016/j.rse.2013.01.023.

He, X., Stamnes, K., Bai, Y., Li, W., Wang, D., 2018. Effects of earth curvature on atmospheric correction for ocean color remote sensing. Remote Sens. Environ. 209, 118–133.

Holben, B., Eck, T., Slutsker, I., Tanré, D., Buis, J., Setzer, A., Vermote, E., Reagan, J., Kaufman, Y., Nakajima, T., Lavenu, F., Jankowiak, I., Smirnov, A., 1998. Aeronet—a federated instrument network and data archive for aerosol characterization. Remote Sens. Environ. 66, 1–16. URL: http://www.sciencedirect.com/science/article/pii/S0034425798000315. https://doi.org/10.1016/S0034-4257(98)00031-5.

Ibrahim, A., Franz, B., Ahmad, Z., Healy, R., Knobelspiesse, K., Gao, B.-C., Proctor, C., Zhai, P.-W., 2018. Atmospheric correction for hyperspectral ocean color retrieval with application to the hyperspectral imager for the coastal ocean (hico). Remote Sens. Environ. 204, 60–75. URL: http://www.sciencedirect.com/science/article/pii/S0034425717305047. https://doi.org/10.1016/j.rse.2017.10.041.

Ioannou, I., Gilerson, A., Gross, B., Moshary, F., Ahmed, S., 2011. Neural network approach to retrieve the inherent optical properties of the ocean from observations of modis. Appl. Opt. 50, 3168–3186. URL: http://ao.osa.org/abstract.cfm?URI=ao-50-19-3168. https://doi.org/10.1364/AO.50.003168.

IOCCG, 2006. Remote Sensing of Inherent Optical Properties: Fundamentals, Tests of Algorithms, and Applications volume No. 5 of Reports of the International Ocean Colour Coordinating Group. IOCCG, Dartmouth, Canada. https://doi.org/10.25607/OBP-96. URL: http://www.ioccg.org/reports/report5.pdf.

IOCCG, 2019. Uncertainties in Ocean Colour Remote Sensing volume No. 18 of Reports of the International Ocean Colour Coordinating Group. IOCCG, Dartmouth, Canada. https://doi.org/10.25607/OBP-696. URL: https://ioccg.org/wp-content/uploads/2019/12/ioccg-report-18-uncertainties-rr.pdf.

Kneizys, F.X., Abreu, L.W., Anderson, G., Chetwynd, J., Shettle, E., Berk, A., Bernstein, L., Roberson, D., Acharya, P., Rothman, L., Selby, J., Gallery, W., Clough, S., 1996. MODTRAN2/3 Report and LOWTRAN 7 Model. Technical Report Phillips Laboratory Hanscom AFB.

Koepke, P., Gasteiger, J., Hess, M., 2015. Technical note: Optical properties of desert aerosol with non-spherical mineral particles: data incorporated to opac. Atmos. Chem. Phys. 15, 5947–5956. URL: https://www.atmos-chem-phys.net/15/5947/2015/. https://doi.org/10.5194/acp-15-5947-2015.

Kou, L., Labrie, D., Chylek, P., 1993. Refractive indices of water and ice in the 0.65- to 2.5-μm spectral range. Appl. Opt. 32, 3531–3540. URL: http://ao.osa.org/abstract.cfm?URI=ao-32-19-3531. https://doi.org/10.1364/AO.32.003531.

Lee, Z., Carder, K.L., Arnone, R.A., 2002. Deriving inherent optical properties from water color: a multiband quasi-analytical algorithm for optically deep waters. Appl. Opt. 41, 5755–5772. URL: http://ao.osa.org/abstract.cfm?URI=ao-41-27-5755. https://doi.org/10.1364/AO.41.005755.

Li, H., He, X., Shanmugam, P., Bai, Y., Wang, D., Huang, H., Zhu, Q., Gong, F., 2019. Semi-analytical algorithms of ocean color remote sensing under high solar zenith angles. Opt. Express 27, A800–A817. URL: http://www.opticsexpress.org/abstract.cfm?URI=oe-27-12-A800. https://doi.org/10.1364/OE.27.00A800.

Lucke, R.L., Corson, M., McGlothlin, N.R., Butcher, S.D., Wood, D.L., Korwan, D.R., Li, R.R., Snyder, W.A., Davis, C.O., Chen, D.T., 2011. Hyperspectral imager for the coastal ocean: instrument description and first images. Appl. Opt. 50, 1501–1516. URL: http://ao.osa.org/abstract.cfm?URI=ao-50-11-1501. https://doi.org/10.1364/AO.50.001501.

Maritorena, S., Siegel, D.A., Peterson, A.R., 2002. Optimization of a semianalytical ocean color model for global-scale applications. Appl. Opt. 41, 2705–2714.

Marshak, A., Herman, J., Adam, S., Karin, B., Carn, S., Cede, A., Geogdzhayev, I., Huang, D., Huang, L.-K., Knyazikhin, Y., Kowalewski, M., Krotkov, N., Lyapustin, A., McPeters, R., Meyer, K.G., Torres, O., Yang, Y., 2018. Earth observations from DSCOVR EPIC instrument. Bull. Am. Meteorol. Soc. 99, 1829–1850. https://doi.org/10.1175/BAMS-D-17-0223.1.

MATLAB, 2018. Version 9.4.0.813654 (R2018a). The Mathworks, Inc, Natick, Massachusetts.

Mélin, F., Zibordi, G., 2010. Vicarious calibration of satellite ocean color sensors at two coastal sites. Appl. Opt. 49, 798–810. URL: http://ao.osa.org/abstract.cfm?URI=ao-49-5-798. https://doi.org/10.1364/AO.49.000798.

Monahan, E.C., Muircheartaigh, I., 1980. Optimal power-law description of oceanic whitecap coverage dependence on wind speed. J. Phys. Oceanogr. 10, 2094–2099. https://doi.org/10.1175/1520-0485(1980)010<2094:OPLDOO>2.0.CO;2.

Moon, J.-E., Park, Y.-J., Ryu, J.-H., Choi, J.-K., Ahn, J.-H., Min, J.-E., Son, Y.-B., Lee, S.-J., Han, H.-J., Ahn, Y.-H., 2012. Initial validation of goci water products against in situ data collected around korean peninsula for 2010–2011. Ocean Sci. J. 47, 261–277. https://doi.org/10.1007/s12601-012-0027-1.

Morel, A., Antoine, D., Gentili, B., 2002. Bidirectional reflectance of oceanic waters: accounting for raman emission and varying particle scattering phase function. Appl. Opt. 41, 6289–6306. URL: http://ao.osa.org/abstract.cfm?URI=ao-41-30-6289. https://doi.org/10.1364/AO.41.006289.

Neumaier, A., 1998. Solving ill-conditioned and singular linear systems: a tutorial on regularization. SIAM Rev. 40, 636–666. https://doi.org/10.1137/S0036144597321909.

Nordkvist, K., Loisel, H., Gaurier, L.D., 2009. Cloud masking of seawifs images over coastal waters using spectral variability. Opt. Express 17, 12246–12258. URL: http://www.opticsexpress.org/abstract.cfm?URI=oe-17-15-12246. https://doi.org/10.1364/OE.17.012246.

Ottaviani, M., Spurr, R., Stamnes, K., Li, W., Su, W., Wiscombe, W., 2008. Improving the description of sunglint for accurate prediction of remotely sensed radiances. J. Quant. Spectrosc. Radiat. Transf. 109, 2364–2375.

Pahlevan, N., Lee, Z., Wei, J., Schaaf, C.B., Schott, J.R., Berk, A., 2014. On-orbit radiometric characterization of oli (landsat-8) for applications in aquatic remote sensing. Remote Sens. Environ. 154, 272–284. https://doi.org/10.1016/j.rse.2014.08.001.

Pahlevan, N., Roger, J.-C., Ahmad, Z., 2017a. Revisiting short-wave-infrared (swir) bands for atmospheric correction in coastal waters. Opt. Express 25, 6015–6035. URL: http://www.opticsexpress.org/abstract.cfm?URI=oe-25-6-6015. https://doi.org/10.1364/OE.25.006015.

Pahlevan, N., Sarkar, S., Franz, B., Balasubramanian, S., He, J., 2017b. Sentinel-2 multispectral instrument (msi) data processing for aquatic science applications: demonstrations and validations. Remote Sens. Environ. 201, 47–56. URL: http://www.sciencedirect.com/science/article/pii/S0034425717303991. https://doi.org/10.1016/j.rse.2017.08.033.

Patt, F., Barnes Jr., R., Franz, B., Robinson, W., Feldman, G., Bailey, S., Gales, J., Werdell, P., Wang, M., Frouin, R., Stumpf, R., Arnone Jr., R., Martinolich, P., Ransibrahmanakul, V., O'Reilly, J., Yoder, J., 2003. Algorithm Updates for the Fourth SeaWiFS Data Reprocessing, NASA Tech. Memo. 2003–206892. Technical Report NASA Goddard Space Flight Center College Park, MD.

Pedregosa, F., Varoquaux, G., Gramfort, A., Michel, V., Thirion, B., Grisel, O., Blondel, M., Prettenhofer, P., Weiss, R., Dubourg, V., Vanderplas, J., Passos, A., Cournapeau, D., Brucher, M., Perrot, M., Duchesnay, E., 2011. Scikit-learn: machine learning in Python. J. Mach. Learn. Res. 12, 2825–2830.

Pekel, J.-F., Cottam, A., Gorelick, N., Belward, A.S., 2016. High-resolution mapping of global surface water and its long-term changes. Nature 540, 418–422. https://doi.org/10.1038/nature20584.

Pope, R.M., Fry, E.S., 1997. Absorption spectrum (380–700 nm) of pure water. ii. integrating cavity measurements. Appl. Opt. 36, 8710–8723. URL: http://ao.osa.org/abstract.cfm?URI=ao-36-33-8710. https://doi.org/10.1364/AO.36.008710.

Prechelt, L., 1997. Early stopping - but when?. In: Neural Networks: Tricks of the Trade, Volume 1524 of LNCS, Chapter 2. Springer-Verlag, pp. 55–69.

Qi, L., Lee, Z., Hu, C., Wang, M., 2017. Requirement of minimal signal-to-noise ratios of ocean color sensors and uncertainties of ocean color products. J. Geophys. Res. Oceans 122, 2595–2611.

Reynolds, R.A., Stramski, D., Neukermans, G., 2016. Optical backscattering by particles in arctic seawater and relationships to particle mass concentration, size distribution, and bulk composition. Limnol. Oceanogr. 61, 1869–1890. https://doi.org/10.1002/lno.10341.

Ruddick, K., 2010. Due Coastcolour Round Robin Protocol. URL: http://www.coastcolour.org/documents/Coastcolour-RRP-v1.2.pdf.

Smith, R.C., Baker, K.S., 1981. Optical properties of the clearest natural waters (200–800 nm). Appl. Opt. 20, 177–184. URL: http://ao.osa.org/abstract.cfm?URI=ao-20-2-177. https://doi.org/10.1364/AO.20.000177.

Smyth, T.J., Moore, G.F., Hirata, T., Aiken, J., 2006. Semianalytical model for the derivation of ocean color inherent optical properties: description, implementation, and performance assessment. Appl. Opt. 45, 8116–8131. URL: http://ao.osa.org/abstract.cfm?URI=ao-45-31-8116. https://doi.org/10.1364/AO.45.008116.

Stamnes, K., Stamnes, J.J., 2016. Radiative Transfer in Coupled Environmental Systems: An Introduction to Forward and Inverse Modeling. John Wiley & Sons.

Stamnes, K., Thomas, G.E., Stamnes, J.J., 2017. Radiative Transfer in the Atmosphere and Ocean, second ed. Cambridge University Press.

Stamnes, K., Hamre, B., Stamnes, S., Chen, N., Fan, Y., Li, W., Lin, Z., Stamnes, J., 2018a. Progress in forward-inverse modeling based on radiative transfer tools for coupled atmosphere-snow/ice-ocean systems: a review and description of the accurt model. Appl. Sci. 8, 2682.

Stamnes, S., Fan, Y., Chen, N., Li, W., Tanikawa, T., Lin, Z., Liu, X., Burton, S., Omar, A., Stamnes, J., Cairns, B., Stamnes, K., 2018b. Advantages of measuring the q stokes parameter in addition to the total radiance i in the detection of absorbing aerosols. Front. Earth Sci. 6, 1–11.

Stamnes, S., Hostetler, C., Ferrari, R., Burton, S., Lui, X., Hair, J., Hu, Y., Wasilewski, A., Martin, W., Van Diedenhoven, B., Chowdhary, J., Cetinic, L., Berg, L.K., Stamnes, K., Cairns, B., 2018c. Simultaneous polarimeter retrievals of microphysical aerosol and ocean color parameters from the mapp algorithm with comparison to high spectral resolution lidar aerosol and ocean products. Appl. Opt. 57, 2394–2413.

Stramska, M., Petelski, T., 2003. Observations of oceanic whitecaps in the north polar waters of the Atlantic. J. Geophys. Res. Oceans 108. https://doi.org/10.1029/2002JC001321. 3086 n/a–n/a. URL: https://doi.org/10.1029/2002JC001321.

Voss, K.J., Morel, A., Antoine, D., 2007. Detailed validation of the bidirectional effect in various case 1 waters for application to ocean color imagery. Biogeosciences 4, 781–789. URL: https://www.biogeosciences.net/4/781/2007/. https://doi.org/10.5194/bg-4-781-2007.

Wang, M., 2002. The rayleigh lookup tables for the seawifs data processing: Accounting for the effects of ocean surface roughness. Int. J. Remote Sens. 23, 2693–2702. URL: https://doi.org/10.1080/01431160110115591 https://doi.org/10.1080/01431160110115591.

Wang, M., 2005. A refinement for the rayleigh radiance computation with variation of the atmospheric pressure. Int. J. Remote Sens. 26, 5651–5663. URL: https://doi.org/10.1080/01431160500168793. https://doi.org/10.1080/01431160500168793.

Wang, M., Bailey, S.W., 2001. Correction of sun glint contamination on the seawifs ocean and atmosphere products. Appl. Opt. 40, 4790–4798. URL: http://ao.osa.org/abstract.cfm?URI=ao-40-27-4790. https://doi.org/10.1364/AO.40.004790.

Wang, M., Shi, W., 2006. Cloud masking for ocean color data processing in the coastal regions. IEEE Trans. Geosci. Remote Sens. 44 https://doi.org/10.1109/TGRS.2006.876293 (3196–3105).

Werdell, P.J., Fargion, G.S., McClain, C.R., Bailey, S.W., 2002. The Seawifs Bio-Optical Archive and Storage System (Seabass): Current Architecture and Implementation.

Werdell, P.J., Bailey, S.W., Franz, B.A., Morel, A., McClain, C.R., 2007. On-orbit vicarious calibration of ocean color sensors using an ocean surface reflectance model. Appl. Opt. 46, 5649–5666. URL: http://ao.osa.org/abstract.cfm?URI=ao-46-23-5649. https://doi.org/10.1364/AO.46.005649.

Werdell, P.J., Franz, B.A., Bailey, S.W., Feldman, G.C., Boss, E., Brando, V.E., Dowell, M., Hirata, T., Lavender, S.J., Lee, Z., Loisel, H., Maritorena, S., Mélin, F., Moore, T.S., Smyth, T.J., Antoine, D., Devred, E., d'Andon, O.H.F., Mangin, A., 2013. Generalized Ocean color inversion model for retrieving marine inherent optical properties. Appl. Opt. 52, 2019–2037. https://doi.org/10.1364/AO.52.002019.

Wessel, P., Smith, W.H.F., 1996. A global, self-consistent, hierarchical, high-resolution shoreline database. J. Geophys. Res. Solid Earth 101, 8741–8743. URL. https://agupubs.onlinelibrary.wiley.com/doi/abs/10.1029/96JB00104. https://doi.org/10.1029/96JB00104. arXiv. https://agupubs.onlinelibrary.wiley.com/doi/pdf/10.1029/96JB00104.

Zibordi, G., Mélin, F., Cois Berthon, J.-F., Holben, B., Slutsker, I., Giles, D., D'Alimonte, D., Vandemark, D, Feng, H., Schuster, G., Fabbri, B.E., Kaitala, S, Seppälä, J, 2009. Aeronet-oc: A network for the validation of ocean color primary products. J. Atmos. Ocean. Technol. 26, 1634–1651. URL: https://doi.org/10.1175/2009JTECHO654.1 https://doi.org/10.1175/2009JTECHO654.1.